UNIVERSIDADE D
COIMBRA

Tiago André Rodrigues Narciso

ANALYSIS OF FATIGUE CRACK PROPAGATION ON LOAD PATTERNS PRODUCED BY TRAINS ON RAILWAY BRIDGES

Dissertação no âmbito do Mestrado em Engenharia Mecânica, na especialidade de Produção e Projeto orientada pelo Professor Doutor Diogo Mariano Simões Neto e pelo Mestre Edmundo Rafael de Andrade Sérgio e apresentada ao Departamento de Engenharia Mecânica da Faculdade de Ciências e Tecnologia da Universidade de Coimbra.

Julho de 2024

FACULDADE DE CIÊNCIAS E TECNOLOGIA
UNIVERSIDADE D COIMBRA

Analysis of fatigue crack propagation on load patterns produced by trains on railway bridges

A dissertation submitted in partial fulfilment of the requirements for the degree of Master in Mechanical Engineering in the speciality of Manufacturing and Design.

Análise da propagação de fendas por fadiga em padrões de carga produzidos por comboios em pontes ferroviárias

Author

Tiago André Rodrigues Narciso

Advisors

Professor Doutor Diogo Mariano Simões Neto

Mestre Edmundo Rafael de Andrade Sérgio

Committee

Chair	**Professor Doutor Ricardo Nuno Madeira Soares Branco** **Professor Auxiliar da Universidade de Coimbra**
Member	**Professor Doutor Luís Filipe Borrego** **Professor do Instituto Superior de Engenharia de Coimbra**
Advisor	**Mestre Edmundo Rafael de Andrade Sérgio** **Assistente Convidado da Universidade de Coimbra**

Coimbra, July, 2024

“Doubt is the beginning of wisdom”

Aristóteles

ACKNOWLEDGEMENTS

I would like to express my gratitude to the people who have crossed my path, without whom this journey would not be so remarkable.

To Professor Diogo Neto, I truly thank you for all the help and support along my academic journey. All the knowledge, availability and patience were essential for conclude this dissertation.

To Mestre Edmundo Sérgio for his help and availability in the completion of this work, and for being always ready to help, even in the most difficult times.

To Professor Fernando Antunes, for all your words of encouragement and for always being available to help and share knowledge. For being a source of inspiration this semester.

To the Technology Group of Mechanical Engineering Department for the availability of the finite element program, DD3IMP.

To my parents for giving me the chance to have this fantastic journey. To my parents, brother and the rest of my family for supporting me whenever I needed it.

To my girlfriend, Patrícia, for all the motivation and support she has given me during this journey and for always being by my side when I needed her most.

To my dearest friends, Bruno, Carolina, Henrique, José and Maria Inês, for all the study sessions, academic dinners, nights out, conversations and company over the past five years.

To my Board, Bea, Bé, Patrícia and Ticha, for helping me to have an extra-curricular experience at BEST Coimbra that I will carry with me for the rest of my life. BEST Coimbra for developing me as a person and enriching my personal growth. Thank you to everyone who has been part of this organisation.

To my “padrinhos”, “afilhados” and the rest of the praxis family for helping me to be involved in the academic traditions of Coimbra. Thank you for making this city magical and special.

Abstract

Most mechanical components are subjected to cyclic or dynamic loads that can cause them to fail. Fatigue is the most common failure phenomenon in components exposed to these conditions. Therefore, to avoid failures with very serious consequences, it is important to design components for fatigue and predict their service life. Life prediction is usually studied based on the evolution of Fatigue Crack Growth (FCG) using the da/dN-ΔK curves. However, this approach has some limitations because the phenomena that occur at the crack tip are irreversible and operate in the plastic domain, while the stress intensity factor, ΔK, is a purely elastic parameter. To overcome this limitation, other non-linear parameters have been proposed, one of which is the plastic Crack Tip Opening Displacement (CTOD), which will be discussed in this study to explain some phenomena that occur in fatigue crack propagation.

The main objective of this thesis is to analyse the effect of variable amplitude loading on fatigue crack propagation, in Compact Tension (CT) specimens made from an AA2024-T351 alloy. This work focused on complex loading, so two real loads of trains passing over railway bridges were studied. The loads were filtered using the Rainflow method. The Finite Element Method (FEM) was used to solve the problem and the Finite Element program DD3IMP was used to simulate the results numerically. The two loads were also compared with constant loads to analyse possible similarities that could simplify the study of complex loads. The importance of crack closure was considered in this study by numerically analysing the two complex loads in a hypothetical situation where the contact between the flanks of the CT specimens was not considered. The influence of elastic cycles on the pattern was tested by comparing the main load with another one, in which these cycles were omitted.

It was concluded from this study that crack closure is a very important factor for complex loads with high amplitude values. It was also found that the omission of elastic cycles has practically no effect on fatigue crack propagation, which is a simplification in the analysis of complex loads.

Keywords: Fatigue Crack Growth, Variable Amplitude Loading, Complex Loadings, Numerical Simulation, Crack Closure.

Resumo

A maioria dos componentes mecânicos está sujeita a cargas cíclicas ou dinâmicas que podem provocar fenómenos de falhas destes componentes. A fadiga é o fenómeno de falha mais comum em componentes sujeitos a estas condições. Deste modo é importante dimensionar os componentes à fadiga e prever a sua vida útil para evitar falhas com consequências muito graves. A previsão da vida útil é normalmente feita a partir da evolução da propagação das fendas por fadiga, onde se utiliza as curvas $da/dN-\Delta K$. No entanto, esta abordagem apresenta sempre algumas limitações porque os fenómenos que acontecem na extremidade da fenda são irreversíveis, atuando no regime plástico, e o fator de intensidade de tensão, ΔK, é um parâmetro meramente elástico. Para contornar esta limitação, outros parâmetros não lineares foram propostos, um deles é o CTOD plástico que vai ser abordado neste trabalho para explicar alguns fenómenos que acontecem na propagação de fendas por fadiga.

Esta dissertação tem como objetivo principal estudar o efeito dos carregamentos de amplitude variável na propagação de fendas por fadiga em provetes de tensão compacta (CT) de uma liga AA2024-T351. Para isso, foram estudados dois carregamentos reais de comboios a passar sobre pontes ferroviárias. Os carregamentos foram filtrados através do método de Rainflow. Recorreu-se à análise de métodos de elementos finitos (MEF) para a resolução do problema, o programa de elementos finitos DD3IMP efetuou a simulação numérica de resultados. Para os dois carregamentos foi ainda feita uma comparação com carregamentos constantes para analisar possíveis semelhanças que podiam simplificar o estudo de carregamentos complexos. A importância do fecho de fenda também foi considerada neste estudo ao analisar numericamente os dois carregamentos complexos numa situação hipotética que se desprezou o contacto entre os flancos dos provetes CT. Também se testou a influência dos ciclos elásticos no padrão, comparando o carregamento principal com outro em que se considerou a omissão destes ciclos.

Com este estudo, conclui-se que o fecho de fenda é um fator bastante importância para os carregamentos complexos com valores de amplitude elevados. Também se verificou que a omissão dos ciclos elásticos praticamente não tem influência na propagação da fenda por fadiga, simplificando a análise de carregamentos complexos.

Palavras-chave: Crescimento de Fendas por Fadiga, Carregamento de Amplitude Variável, Carregamentos Complexos, Simulação Numérica, Fecho de Fenda.

Contents

LIST OF FIGURES

LIST OF TABLES

LIST OF SIMBOLS AND ACRONYMS/ ABBREVIATIONS

List of Symbols

a – Crack length

a_0 – Initial crack length

C,m – Constants of the Paris-Erdogan law

$CTOD_p$ – Crack Opening Displacement plastic

$CTOD_e$ – Crack Opening Displacement elastic

C_X – Parameter of the Frederick-Armstrong kinematic hardening law

da/dN – Fatigue crack growth rate

E – Young Modulus

F – Applied load

F_{max} – Maximum load in a loading cycle

F_{min} – Minimum load in a loading cycle

F_{open} – Crack opening load

$F_{closure}$ – Crack closing load

K – Stress intensity factor

K_{1C} – Fracture toughness

K_{max} – Maximum stress intensity factor

K_{min} – Minimum stress intensity factor

K_{open} – K value corresponding to crack opening

P_{max} – Maximum load in constant amplitude loading

P_{mean} – Mean load value in constant amplitude loading

P_{min} – Minimum load in constant amplitude loading

n – Swift law hardening coefficient

U^*_{open} – Modified crack open level

$U^*_{closure}$ – Modified crack closure level

W – Width of CT specimen

$\dot{X}$– Deviatoric back-stress tensor

X_{sat} – Frederick-Armstrong saturation parameter

Y – Geometric factor

Y_0 – Initial yield stress

ΔK – Stress intensity factor range

ΔK_{eff} – Effective stress intensity factor range

ΔK_{lim_elas} – Elastic limit intensity factor

ΔK_{th} – Fatigue threshold

ΔN – Number of load cycles

ΔP_{eq} – Equivalent load range

$\dot{\bar{\varepsilon}}^{p}$ – Equivalent critical plastic deformation value

$\bar{\varepsilon}^{p}$ – Equivalent plastic strain

$\boldsymbol{\sigma}'$ – Deviatoric Cauchy stress tensor

$\bar{\sigma}$ – Equivalent stress

σ – Nominal stress

σ_{max} – Maximum stress

σ_{min} – Minimum stress

σ_Z – Normal stress component

ν – Poisson's ratio

Acronyms/Abbreviations

AA – Aluminium Alloy

CAL – Constant Amplitude Loading

CJP – Christopher James Patterson (model)

COD – Crack Opening Displacement

CT – Compact-Tension

CTOD – Crack Tip Opening Displacement

DD3IMP – Deep Drawing 3D IMPlicit finite element solver

FCG – Fatigue Crack Growth

LEFM – Linear Elastic Fracture Mechanics

OICC – Oxidation Induced Crack Closure

PICC – Plasticity Induced Crack Closure

RICC – Roughness Induced Crack Closure

VA – Variable Amplitude

VAL – Variable Amplitude Loading

1. INTRODUCTION

1.1. Motivation

Most mechanical components are subjected to cyclic loading, either of constant or variable amplitude (VA). Fatigue is the failure of a component subjected to this type of loading. The prevention of fatigue is a complex process because it depends on many factors such as the load, the geometry, the material, the environmental conditions and many other factors. The damage tolerance approach [1] assumes the presence of initial defects. In this approach, components are designed to allow for small cracks, which are then inspected at regular intervals. Therefore, it is essential to predict fatigue crack growth (FCG).

Experimental testing is useful for understanding and predicting material behaviour under cyclic loading conditions but is time-consuming and costly. As an alternative, numerical simulation provides a detailed, accurate representation of fatigue behaviour, isolates variable effects and facilitates parametric studies. It provides a better understanding of fatigue and is valuable in developing predictive models and improving cyclic material performance.

The mechanism acting at the crack tip must be considered when modelling FCG. The stress intensity factor range (ΔK) is a concept which relates the stress and strain fields occurring near the crack tip. In addition, the fatigue crack growth rate (FCGR) is usually determined by the da/dN-ΔK curves, which are correlated in several propagation laws [2], [3], [4]. Despite its importance, ΔK has some limitations since is an elastic parameter, and fatigue crack propagation is related to nonlinear and irreversible mechanisms that occur at the crack tip zone [5] To overcome these limitations, other approaches have been developed, such as the crack closure concept, T-stress, CJP model, integral J, crack tip dissipated energy and Crack Tip Opening Displacement (CTOD) [6].

Due to the complexity of fatigue phenomena at the crack tip, none of the models is universally accepted. In this study, it is assumed that cyclic plastic deformation is the main damage mechanism and that the cumulative plastic strain at the crack tip is the dominant parameter for FCG. This approach has been verified by comparing numerical predictions with experimental results. Good correlations have been found for overloads [7], load blocks [8] and can be used with confidence to study other complex load patterns [9], [10]. Therefore, the aim of the present work is to study realistic and complex load patterns to identify the

fundamental mechanism of FCG. This way, loading patterns obtained numerically by simulating trains crossing a real bridge were considered [11].

1.2. Objectives

The main aim of this thesis is the study of fatigue crack growth in complex patterns. Different aspects of these main patterns will be studied, such as crack closure, simplification through constant amplitude loading and the omission of cycles. Two different patterns will be studied. The crack propagation is controlled by the cumulative plastic deformation at the crack tip. Numerical simulations consider CT specimen, made from 2024-T351 aluminium alloy. The in-house developed finite element code, DD3IMP, was employed in all the simulations.

1.3. Layout of the thesis

The structure of the thesis is as follows:

- **Chapter 1 -** Introduction: contains the main subject, motivation, objectives and the structure of the thesis.
- **Chapter 2 -** Literature Review: explains the main subjects and some other concepts related to fatigue, including Linear Elastic Fracture Mechanics (LEFM), crack closure, CTOD and blunting. This chapter also introduces some studies of other patterns in the fatigue field, some standard patterns to take as a reference and some software used. Studies that take into account other approaches such as the omission of cycles, the Rainflow method and the Constant Amplitude Loading (CAL) are also presented.
- **Chapter 3 -** Numerical Model: contains information about the plasticity theory and materials employed. The finite element model is described, and the load conditions are presented.
- **Chapter 4 -** Numerical results: presents the results obtained in this study for the two loading patterns and for the different variables of the study, including the effect of contact between the flaks, the simplification to a CAL pattern and omitting cycles.

- **Chapter 5 -** Discussion of results: contains the comparison of some variables for the two load patterns.
- **Chapter 6 –** Conclusion: presents the main conclusions obtained in this study.

2. LITERATURE REVIEW

2.1. Fatigue

2.1.1. Fatigue Phenomenon

Fatigue is a term introduced in the 19th century to describe the failure of a component subjected to a cyclic load below the yield stress [12]. 80% to 90% of failures in mechanical components are due to fatigue [13]. Fatigue is caused by the nucleation of a crack which propagates through the component. Eventually, when the uncracked section of the material cannot support the applied stress, failure occurs. Fatigue can be described in terms of four stages: crack initiation, microscopic growth, crack propagation and ultimate failure.

2.1.2. Linear Elastic Fracture Mechanics

Since crack growth increases cumulatively with the number of cycles applied, predicting fatigue life is extremely important in developing damage tolerant design guidelines. The theory of linear elastic fracture mechanics (LEFM) has been initially proposed by Irwin [14], [15] for the prediction of FCG. This theory has been used to measure the stress distribution around the crack tip. The LEFM approach is acceptable when the region of non-linear behaviour is very small in relation to the length of the crack and the other dimensions of the specimen. The stress near the crack tip could be predicted by linear elasticity theory and described by the stress intensity factor, K [15].

$$K = Y\sigma\sqrt{\pi a,} \tag{2.1}$$

where σ is the nominal stress, a is the crack length and Y is a parameter used to characterize crack length and component geometry. In LEFM theory, FCG is studied using da/dN-ΔK curves as shown in Figure 2.1 [16]. The components are subjected to cyclic loading, so K changes with time, therefore these curves show the evolution of the crack growth rate over the range of the stress intensity factor, ΔK, which is given by the difference between the maximum and minimum values of K in the loading cycle. The stress intensity factor range can be calculated using the following expression:

$$\Delta K = K_{\max} - K_{\min} \tag{2.2}$$

where $K_{\max}$ is the maximum value and $K_{\min}$ is the minimum value of the stress intensity.

Three distinctive zones are represented in Figure 2.1:

- **Region I:** In this region, the rate of crack growth is highly dependent on the stress intensity factor range. Propagation is slow for low stress intensity factors. There is no crack propagation below a ΔK_{th}, known as the fatigue threshold.
- **Region II:** In this zone, stable crack propagation is achieved. The Paris-Erdogan law defines a linear relationship, on log-log scale, between *da/dN*-Δ*K* [2]. Paris-Erdogan law is represented in (2.3), where *C* and *m* are material constants that depend on the environmental conditions and stress ratio.

$$\frac{da}{dN} = C\ (\Delta K)^m, \tag{2.3}$$

- **Region III:** In this region, as Δ*K* increases, there is a quick increase of *da/dN*. The fracture occurs, when the value of $K_{\max}$ reaches the value of material fatigue toughness, K_{IC}.

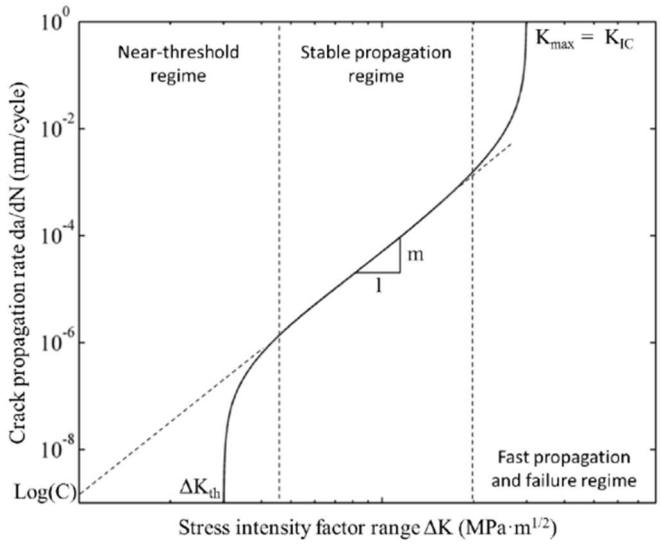

Figure 2.1 *da/dN*–Δ*K* graph, in logarithmic scale. Adapted from [16].

2.1.3. Crack Closure effect

FCG is related to nonlinear and irreversible mechanisms happening at the crack tip. This limits the LEFM theory because one of the pillars is ΔK, which is an elastic parameter [17]. The crack-closure concept, introduced by Elber [18], [19] is used to study FCG in a

more accurate way and to suppress some of the gaps left by LEFM. Accordingly, Elber included in the models an effective stress intensity factor, $\Delta K_{eff,}$ given by:

$$\Delta K_{\text{eff}} = K_{\max} - K_{\text{open}} \tag{2.4}$$

where K_{open} represents the stress intensity factor below which the crack remains closed.

Crack closure can explain the influence of mean stress in both Regime I and II of crack propagation [20] and the transient crack growth behaviour after overloads [21]. Ritchie *et al.* in 1980 [22], [23], [24] and Suresh and Ritchie in 1982 [23], [24] identified the following main mechanisms for closing cracks: PICC (plasticity induced crack closure), OICC (oxide-induced crack closure) and RICC (roughness-induced crack closure). PICC is the most important mechanism in Regime II [20].

A numerical approach was adopted by Borges *et al.*[5] to predict FCG rate, assuming that cyclic plastic deformation is the major cause of damage and using a cumulative plastic strain as the crack driving parameter. ΔK was found to control crack tip damage. The analysis of FCG after an overload with and without contact of crack flanks showed that the typical variation of da/dN observed is linked to crack closure variations. However, the analysis of crack tip plastic deformation also shows that there is crack tip damage below closure; therefore, the definition of an effective load range $\Delta K_{\text{eff}} = K_{\max} - K_{\text{open}}$ is not the most correct.

2.1.4. Crack Tip Opening Displacement

In 1961, Wells introduced the concept of Crack Tip Opening Displacement (CTOD) [25]. This parameter is used to measure the displacement of the crack flanks. Wells [25] proposed a definition that concentrates on the opening displacement of the original crack tip, while Rice [26], years later, developed a method that consists in measuring the displacement at an intersection of a 90° vertex with the slits of the slit. The two definitions are represented in Figure 2.2.

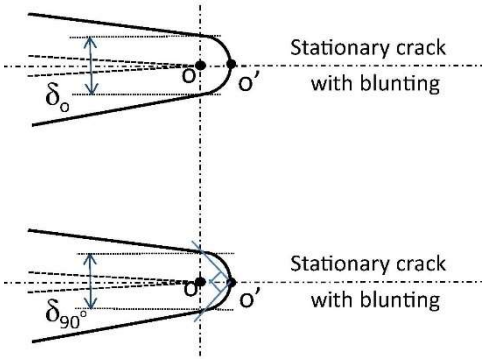

Figure 2.2 Definitions of CTOD. Adapted from[27].

Antunes *et al.* [28], [29] propose to replace the parameter ΔK with a new concept, the plastic CTOD ($CTOD_p$). This model considers crack closure at the crack tip and excludes the elastic regime as it does not contribute to FCG [17].

2.1.5. Blunting

Crack closure mechanism has a significant impact on the effects of overload [21], [30]. One of the models that has been proposed to explain the mechanism of crack growth under cyclic loading is the crack tip blunting model, in which crack growth is associated with blunting in the loading cycle followed by re-sharpening of the crack tip during unloading [31], [32], [33]. Accordingly, Tvergaard [34] compared results for purely cyclic loading with predictions for cases where an overload is applied and stated that crack growth slows significantly after the overload, as it shown in Figure 2.3 [35]. This effect is due to increased blunting at the tip of the crack, which reduces the stress concentration and retards crack propagation [21], [36], [37].

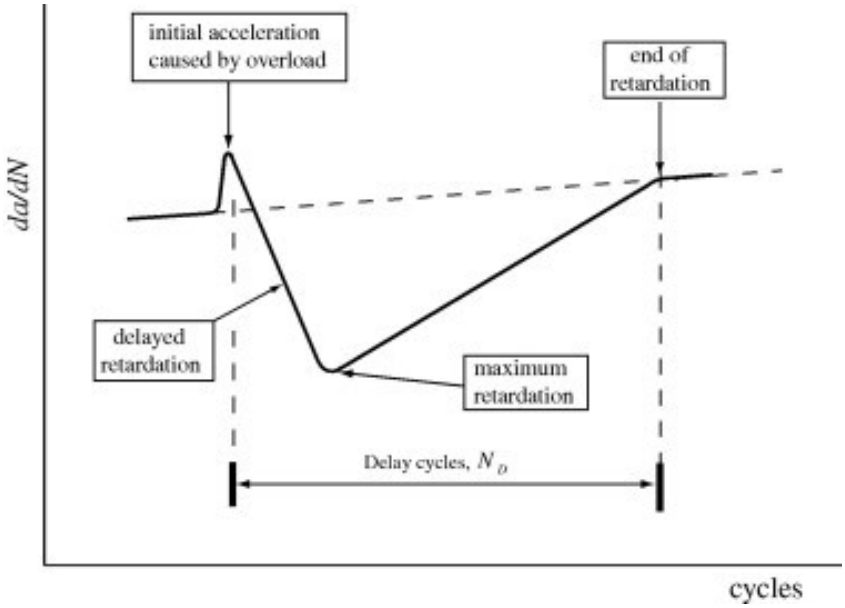

Figure 2.3 Schematic representation of the crack propagation rate as a function of load cycles showing the effect of single tensile overloads on the crack growth rate. Adapted from [35].

The model proposed by Zheng *et al.* [38] is capable of quantitatively predicting the crack acceleration effects under different underload levels and different constant amplitude load ΔK levels following the application of a single underload. Ward-Close *et al*. [39] also postulated that the immediate effect of tensile overload is the plastic blunting of the initially sharp crack. As the crack propagates ahead of the overload position, a hump is left in the crack profile as seen in Figure 2.4 [36].

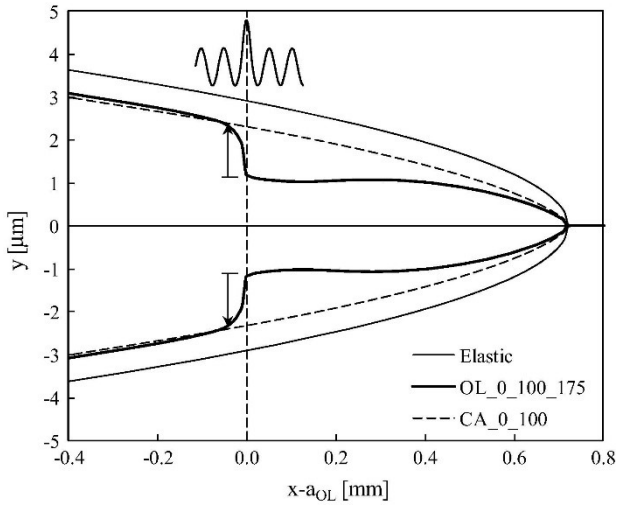

Figure 2.4 Crack profiles during an overload zone. Adapted from [36].

2.2. Complex loading patterns

The purpose of this review is to have a look at the strategies for the analysis of real load patterns. Considering the complexity of the load variations, this is a very challenging task. In this section an overview is presented of the investigations carried out on fatigue behaviour under VA loading, mainly on aluminium and steel alloys.

2.2.1. Standard Patterns

The impact of loading parameters has been widely studied but is not fully understand. In practice, the loads applied to components and structures are typically complex, with variable frequency and amplitude. Standard load patterns have been defined for various practical applications to facilitate comparison of results [40], [41]. CARLOS load pattern was defined for automotive applications, WISPER was the loading sequence suggested for wind turbines, while TWIST, Mini TWIST and FALSTAFF sequences were proposed for transport and fighter aircraft [42]. HELIX/FELIX and the two TURBISTAN sequences are examples proposed for the aerospace field.

2.2.2. Real load patterns

One of the obstacles to predict FCG rate in the real load pattern is the acquisition of real loading pattern. Systems have been implemented in machines and structures, like aircrafts [43], [44] train axles [45], and highway bridges [46] to simplify the study of real load patterns. Besides, numerical models can be used to generate the load patterns [11]. Yamamoto *et al.* [45] measured the operational load-time history of the axles of trains travelling on conventional railway lines. Axle stress was measured using strain gauges attached to the axle body. Railway axle failure can cause critical accidents such as vehicle derailment, therefore axle integrity is a critical aspect of railway safety.

J. Silva [44] instrumented one of the Epsilon TB30 aircraft, having been monitored about 70 flight hours that allowed load factors values in the aircraft centre of gravity and stress values in the aircraft main spar to be recorded. He *et al*. [47] investigated the effect of stress ratio of combined high and low amplitude loading on fatigue life of AISI 316 stainless steel components and concluded that low amplitude cycles following high amplitude cycles contributed to fatigue damage and influenced fatigue life.

2.2.3. Software tools

There are a few software tools to study the FCG [48]. One of them, FASTRAN was written and maintained by Newman at NASA. It uses linear elastic fracture mechanics (LEFM) to model crack propagation under cyclic loading, accounting for overload and underload effects [49]. AFGROW is another software toll and was developed by James A. Harter and Analytical Services and Materials at the US Air Force Research Laboratory. AFGROW closure model was based in some previous works [50], [51], [52] and focuses on empirical data to predict crack growth rates using experimental fatigue crack growth curves. The closure model accounts for varying stress ratios and uses a closure factor to determine the opening stress.

2.3. Load pattern simplification methods

2.3.1. Omission method

Heuler *et al.* [53] used original and modified standard load spectra, namely EC9, TWIST and MiniTWIST, to perform VA fatigue tests on aluminium and steel specimens. The modification to the original spectra consisted of omitting small cycles below the fatigue limit of the material based on local stresses. The authors concluded that this modification of the spectra resulted in crack initiation lives that were 10% to 55% longer and crack propagation lives that were up to 90% longer, demonstrating the influence of cycles with amplitudes below the fatigue limit. He *et al.* [47] investigated the effect of stress ratio of combined high and low amplitude loading on fatigue life of AISI 316 stainless steel components, concluding that low amplitude cycles following high amplitude cycles contributed to the fatigue damage and affected fatigue life. A fatigue life prediction method was proposed considering low amplitude loading below the fatigue limit which was experimentally verified by random amplitude loading tests.

2.3.2. Rainflow method

Matsuishi *et al.* [54] introduced the Rainflow method in 1968, which overcomes the challenge of accurately capturing all cycles, including low-range load cycles that are often omitted in traditional cycle omission counting methods. This approach ensures more accurate and efficient fatigue life predictions, which are critical for optimising engineering

designs and maintenance strategies while conserving resources. Currently there are several different algorithms for the Rainflow Cycle counting method, such as the three-point [48], [49] and four-point cycle counting techniques [50].

Many algorithms have been used to define the varying loads using power spectra, Downing and Socie created one of the most widely referenced and utilized Rainflow cycle-counting algorithms in 1982 [55]. This is an example of three-point cycle counting, but there are others using the same technique [56] and using four-point cycle counting methods [57]. The rule for counting the points is shown in Figure 2.5. The count starts from the peak or valley with the largest absolute value. The cycle identification rule is then applied to check three consecutive points from the first cycle until a closed cycle is defined [58]. The procedure is repeated until the end of the remaining data.

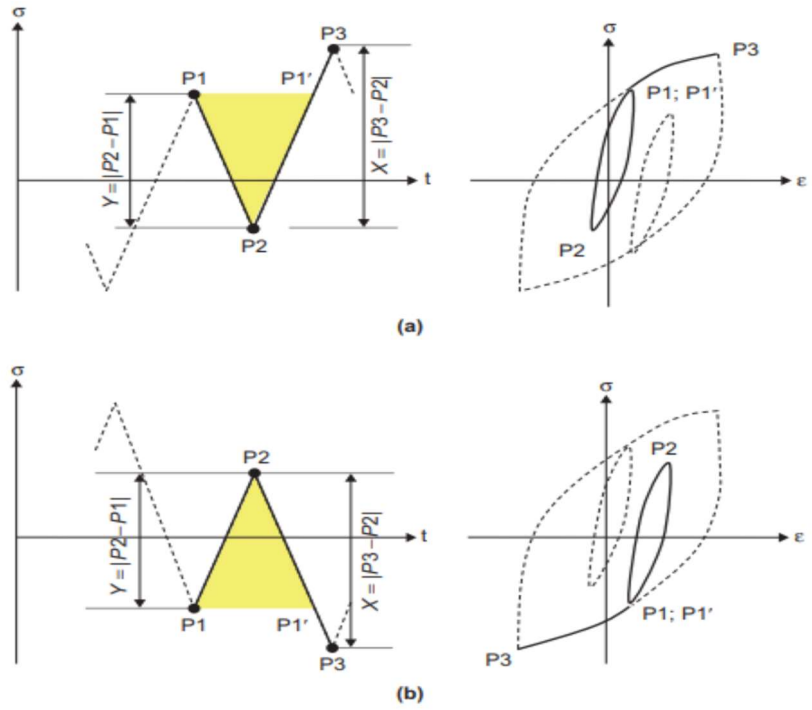

Figure 2.5 The three-point Rainflow cycle counting rule: (a) Hanging cycle, (b) Standing cycle. Adapted from [58].

2.3.3. Constant amplitude loading

The numerical analysis or experimental testing of a real load pattern can be quite time consuming and expensive. Therefore, real load patterns are usually simplified to eliminate non-damaging cycles. Some analyses have been conducted on the axle damage tolerance using CAL spectrums. Beretta *et al*. [59] and Rieger *et al.* [60] claimed that variable amplitude load (VAL) influenced the crack propagation in the axle material, and then

concluded that the full-scale railway axle had a retarding effect. The effect of the VAL series and the length of the load block on crack retardation and acceleration was further investigated by Luke *et al.* [61], [62].

Aursand *et al.* [63] observed in a 62-year period (1957-2019) a mooring system in the North Sea. The load history was condensed and developed into a VAL characteristic load sequence. A validation of a linear damage rule hypothesis was investigated. A constant amplitude loading was tested to verify the similarity with the real loading sequence.

3. NUMERICAL MODEL

3.1. Compact Tension Specimen

In this study, the numerical tests were performed using a Compact Tension (CT) specimen. The CT specimen present a initial crack length, a_0, of 15 mm and a width, W, of 36 mm. Since the CT specimen has two planes of symmetry, only 1/4 of the geometry was modelled. To reduce the computational cost, only one layer of elements was considered in the thickness direction, resulting in a specimen thickness of 0.1 mm. The geometry of the CT specimen is presented in Figure 3.1.

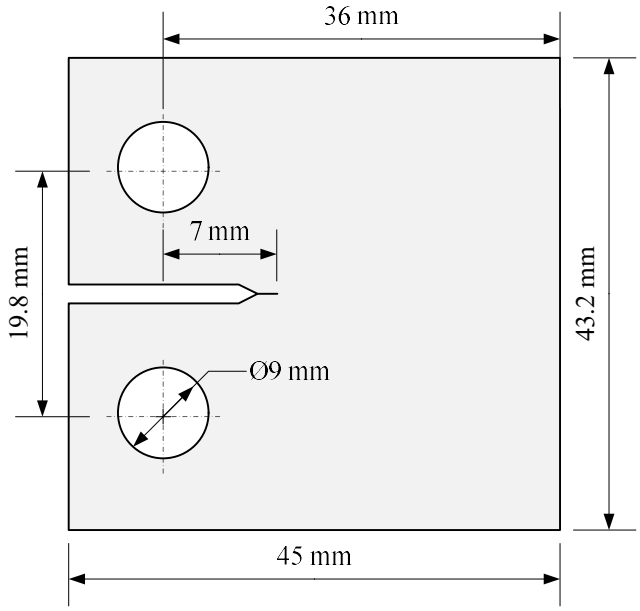

Figure 3.1 Geometry and main dimensions (in mm) of the Compact Tension specimen used in the study of the AA2024-T351.

3.2. Load Patterns

During this study, two Load Patterns (A and B) were performed to see the similarities and differences between each one. Both present a variable amplitude load (VAL) pattern. The load patterns were obtained by studying trains at railway points. There are two patterns, pattern A and pattern B, which involve two different trains and the forces applied under a particular point of the bridge as the train passes. Only one passage is simulated in this pattern, and this pattern will be repeated several times during the life of the bridge. The weight of

the bridge is not considered in this simulation. The patterns are simplified using the Rainflow method of the standard ASMT E 1049[64].

3.2.1. Load Pattern A

The first pattern to be studied is pattern A, shown in Figure 3.2. 57 load cycles define this load block. This pattern was repeated several times throughout the test. The loading factors applied to the CT specimen for pattern A are shown in Annex A. The pattern shown in Figure 3.3 was obtained by applying a multiplication factor of 60.90 N.

This load block can be divided in two zones. The first zone (until 50 load cycles) is composed by small and medium amplitude cycles. At the final part of the block, there is an overload zone which has an amplitude force of 58.27 N.

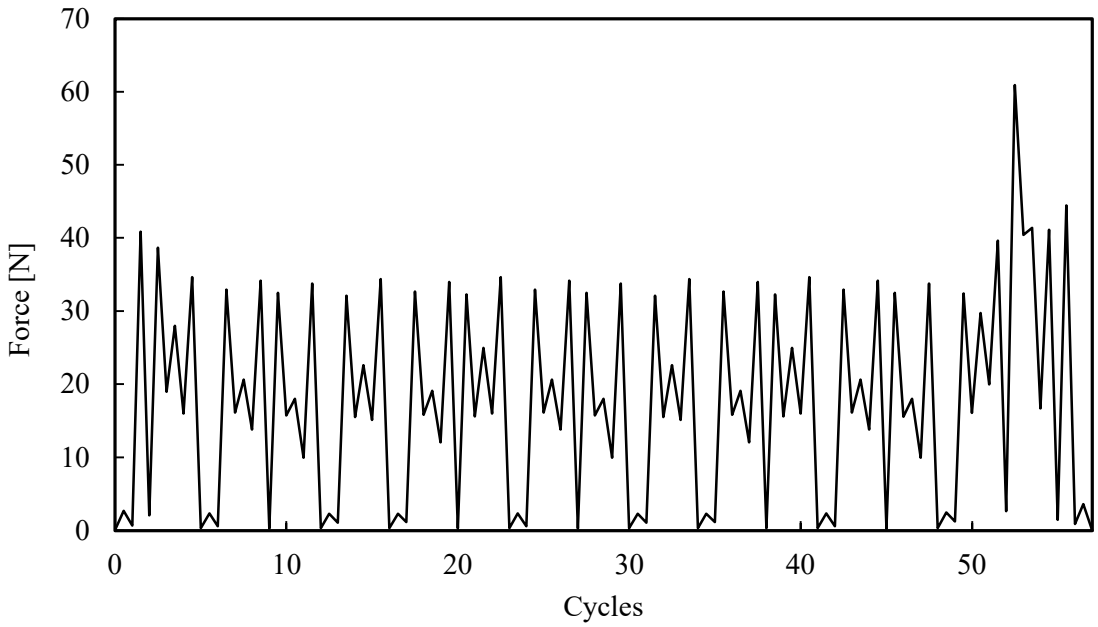

Figure 3.2 Load Pattern A.

3.2.2. Load Pattern B

Pattern B is the second pattern to be studied and is shown in the Figure 3.3. This pattern has 85 load cycles and is also repeated several times. This pattern has less variation in amplitude than pattern A, but the average of the magnitude of the force is higher than pattern A. Most of the values are between 25 N and 50 N. This pattern does not have any overload zones during the block. The loading factors applied to the CT specimen for pattern B are

shown in Annex B. The pattern shown in Figure 3.3 was obtained by applying a multiplication factor of 52.17 N

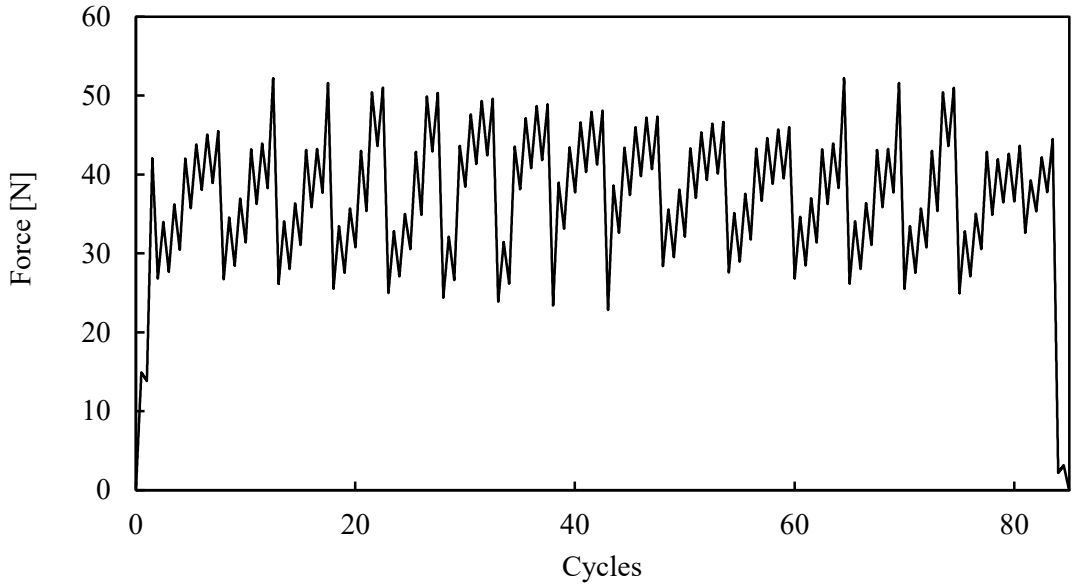

Figure 3.3 Load Pattern B.

3.3. Material Constitutive Model

The material used in this study is the 2024-T351 aluminium alloy, it is a high strength material with adequate workability, hardenability after heat treatment, good machinability and good surface finish. It is widely used in aircraft accessories, gears and shafts, screws, watch parts and computer parts. The chemical composition of AA 2024-T351 is presented in Table 1 [65]. The balance is Aluminium.

Table 1. Chemical composition for 2024-T351 aluminium alloy, in weight (%)

Material	Si	Fe	Cu	Mn	Mg	Cr	Zn	Ti
wt %	0.5	0.5	3.8-4.9	0.30-0.9	1.2-1.8	0.10	0.25	0.15

The elastic behaviour was defined by the Hooke's law, using the Young modulus (E) and Poisson ratio (ν), both listed in Table 2. The plastic behaviour was described with the von Mises yield criterion coupled with a mixed hardening model using the Swift isotropic and Frederick-Armstrong kinematic hardening laws, under an associated flow rule. The Swift isotropic hardening law [66] is given by:

$$Y=C\left[\left(\frac{Y_0}{C}\right)^{\frac{1}{n}}+\bar{\varepsilon}^p\right]^n, \tag{3.1}$$

where Y is the flow stress and $\bar{\varepsilon}^p$ denotes the equivalent plastic strain. The material parameters of Swift law are Y_0, C and n. The Frederick-Armstrong law describes the non-linear kinematic hardening as follows [67], [68]:

$$\dot{\boldsymbol{X}}=C_x\left[X_{Sat}\frac{\boldsymbol{\sigma'}-\boldsymbol{X}}{\bar{\sigma}}-\boldsymbol{X}\right]\dot{\bar{\varepsilon}}^p, \tag{3.2}$$

where $\dot{\boldsymbol{X}}$ is the back-stress tensor, $\bar{\sigma}$ is the equivalent stress and $\dot{\bar{\varepsilon}}^p$ is the equivalent plastic strain rate. C_X and X_{Sat} are the material parameters of Frederick-Armstrong law, which denote the saturation rate and the norm of the saturated back-stress tensor, respectively. The calibration of the material parameters was performed by minimizing the difference between the numerical and the experimental results of stress-strain curves obtained in low cycle fatigue tests. The obtained set of material parameters is presented in Table 2.

Table 2. Elastic-plastic properties for the 2024-T351 aluminium alloy.

E [GPa]	N	Y_0 [MPa]	C [MPa]	N	X_{Sat} [MPa]	C_X
72.26	0.29	288.96	389.0	0.056	111.84	138.80

3.4. Finite element model

The finite element mesh used in the numerical simulations is shown in Figure 3.4 and consisted of 12,590 finite elements and 25,676 nodes. The model used linear hexahedral finite elements, where the size of the finite elements was gradually reduced to obtain a refined mesh near the crack path. In fact, the mesh size near the crack tip was 8 μm, allowing accurate prediction of local strain and stress gradients. The thickness of the specimen is 0.1 mm to assume a plane stress state.

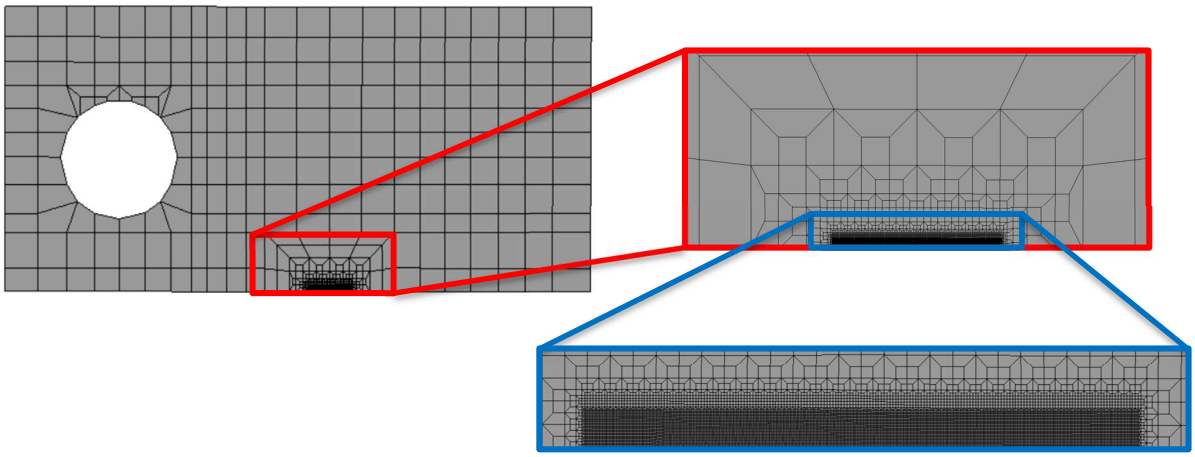

Figure 3.4. Finite element mesh of the CT specimen.

This finite element analysis was performed with the, in-house developed, finite element code DD3IMP, which was originally developed to simulate sheet metal forming processes[69], [70].

3.5. Crack propagation

FCG is simulated here by node release, when the accumulated plastic strain reaches a critical value. The critical value for the cumulative plastic strain at the crack tip for this mesh and material is 1.1, i.e., 110% [71]. This value for 2024-T351 aluminium alloy was previously calibrated by comparing experimental and numerical values of the FCG rate under constant amplitude loading[72]. The equivalent plastic strain is measured at the two Gauss points, behind and ahead the crack tip. The plastic strain value at the crack tip is computed through the average of these two values. The critical plastic strain for a node release is supposed to be a material property. Each crack propagation corresponds to a length of 8μm. The crack propagation is always made at minimum load to avoid converge problems that could arise by propagating the crack at maximum load. The crack growth rate is calculated using:

$$\frac{da}{dN} = \frac{8}{\Delta N}$$

where ΔN is the number of load cycles needed to reach the critical cumulative plastic strain.

4. NUMERICAL RESULTS

4.1. Load Pattern A

4.1.1. Fatigue crack growth rate

Figure 4.1 presents the evolution of FCG rate per cycle of loading (da/dN), with the current crack size for the respective load pattern A. The crack length starts at 15 mm according to the initial crack length of the experimental CT specimen.

Considering the VAL spectrum, the predicted FCG rate decreases at the beginning (until about 15.25 mm of crack length). This decrease is linked with the stabilization of cyclic plastic deformation and with the formation of residual plastic wake responsible for plasticity-induced crack closure. To analyse this load pattern, it is important to achieve a steady state, which is reached at a crack length of 15.55 mm. The increment of FCG usually produced by the increase in crack length is not observed, which is due to the relatively small extent of crack propagation.

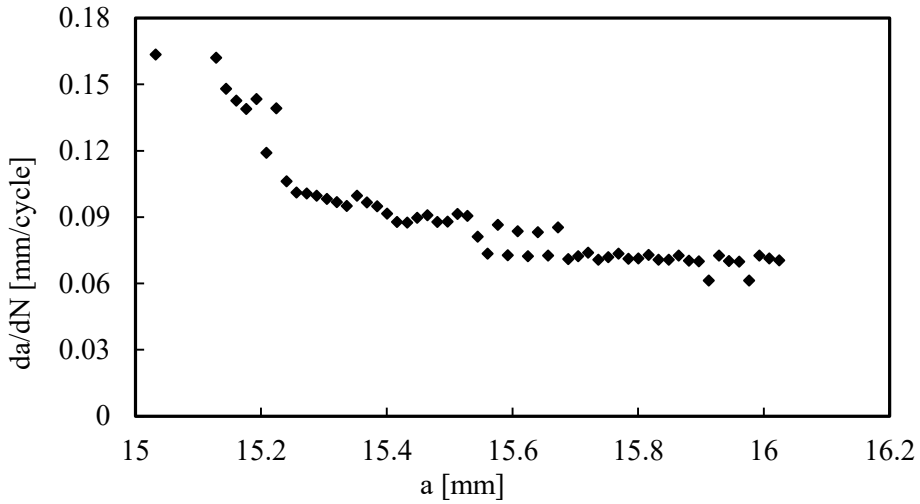

Figure 4.1 Fatigue crack growth rate versus the crack length for the pattern A.

4.1.2. Plastic strain in a load block

The load block shown in Figure 3.2 was repeated several times. It took 98 repetitions of the load block for the crack to reach 15.80 mm. Figure 4.2 represents the 98th load block, which contains 57 cycles, note that no crack propagation occurred in that load block. The

principal vertical axis shows the applied force per cycle and the zones of the load cycles where plastic deformation occurs during the cycles. The secondary axis illustrates the cumulative plastic strain during this load block, at the crack length of 15.80 mm. For this 98th load block, at the beginning of the first cycle, the value of plastic strain is 0.676, at the end of cycle 57 is 1.058. Since the value of plastic strain does not reach 1.1, there is no crack propagation on the 98th load block. Note that, the plastic deformation accumulated during the load block presented is assumed to vary between 0 and 100%. Additionally, Figure 4.2 Cumulative plastic strain and plastic zones in a load block for pattern A. reveals that cycles with small load amplitude exhibit no plastic strain accumulation. Therefore, the rest of the cycles display plastic strain increment at the peaks and the valleys of the cycle. The part of the load cycles where plastic strain occurs during unloading surpasses that during loading.

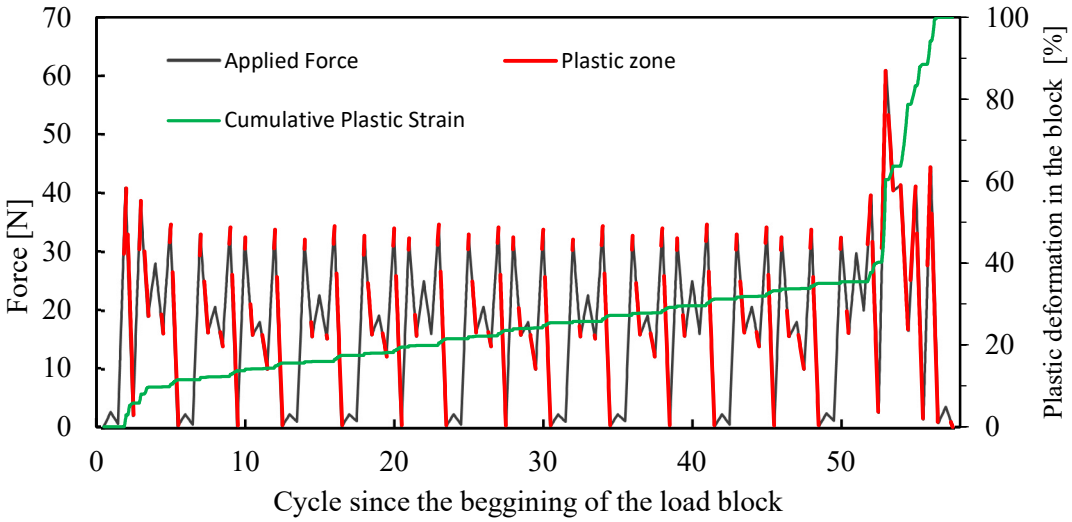

Figure 4.2 Cumulative plastic strain and plastic zones in a load block for pattern A.

The previous results show that 75% of the plastic deformation during the block occurs in the last six cycles, indicating that these final cycles are more crucial for crack propagation than the rest of the load blocks. The application of an overload explains this type of response. Therefore, the pattern was divided into two parts. The first part is composed of cycles between 1 and 51, which comprise the relatively identical load blocks. The results show that, in the first part of the block, plastic strain increases slowly. There is no plastic strain accumulation in small amplitude loading cycles, for example, as occurs in cycle 22 (Figure 4.3a). The second part contains the overload in the cycles between 52 and 57 (Figure 4.3b). At the final part of the block, the cycles with higher loading amplitude occur. Here, the cumulative plastic strain increases quickly with the number of the cycles. The principal

cycle responsible for plastic deformation accumulation is cycle 53, which is the cycle with the highest amplitude loading.

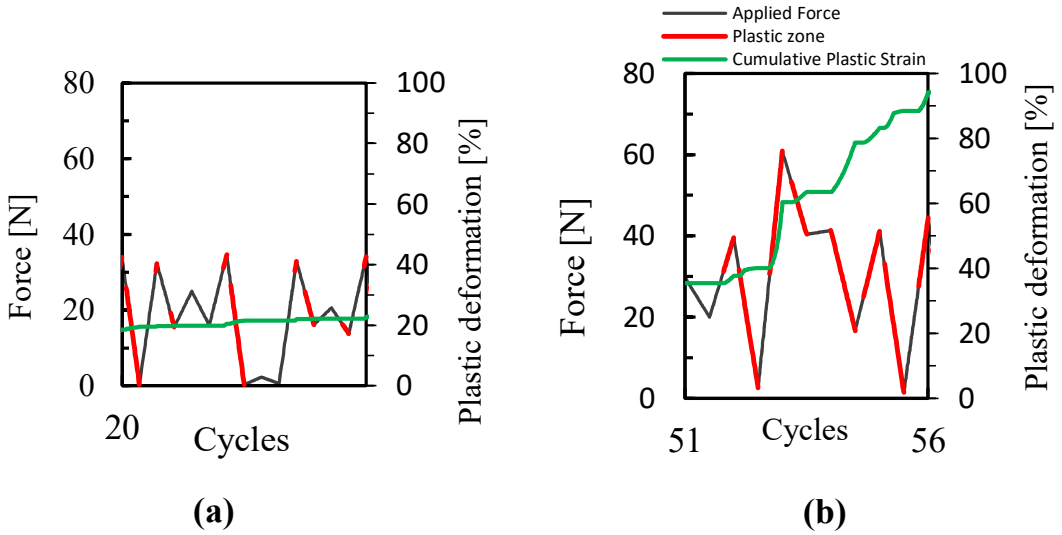

Figure 4.3 Cumulative plastic strain and plastic zones in specific cycles in a loading block. (a) Between 20th and 27th cycle; (b) between cycle 51 and 56.

4.1.3. CTOD of pattern A

Figure 4.4 shows the evolution of the CTOD as a function of the applied force during the 5 critical load cycles of the pattern. It also shows the part of the CTOD in the elastic region $CTOD_e$ and the part in the plastic region $CTOD_p$. The analysis of CTOD plots is very interesting to understand what is happening at the crack tip. The CTOD curve is obtained at the node behind the crack tip, between 52 cycle and 56 cycle of the 98th load block. This includes the overload and is shown in Figure 4.4. The letters in CTOD plot depict the peaks and valleys of the second part of the block (Figure 4.3b).

The analysed five cycles produce different open loops. This indicates that blunting occurs during the cycles. In Figure 4.4 it is possible to identify two distinct loops: one created by the points BCF and the other by the points FGH. The BCF's loop has a larger area and contains the overload. Given this loop, the crack opens at the load of 24.8 N and there is no plastic strain accumulation until the crack opening load. After its opening, the crack enters the elastic domain. At the load of 30.6 N, the plastic deformation begins and increases until the maximum load of 60.90 N is achieved (point C).

The plastic domain of CTOD is represented in Figure 4.4 as $\Delta CTOD_p$. The crack recovers the elastic behaviour when the unloading begins. The elastic behaviour is

represented by straight lines. The slope of the straight lines in the $CTOD_e$ curve is the same for loading and unloading. Until the load of 53.3 N, the curve is linear. After that, the curve shows some plastic deformation until point D. During the path between points D and E, the crack recovers its elastic behaviour due to an increase in the loading. In point E, the unloading restarts, and once again, the crack enters the plastic domain until the crack closes at $F_{closure}$=17.15 N.

The CTOD tends to be bigger for the cycles that have more load amplitude. The amplitude of the cycle which contains the point A during the loading phase is 18.81 N. The amplitude from B to C is 58.27 N. From the cycle that goes from F to G the amplitude is 23.65 N and 42.30 N for the cycle which contains the points H and J. According to this, the amplitude of the loading is more important than the value of the load.

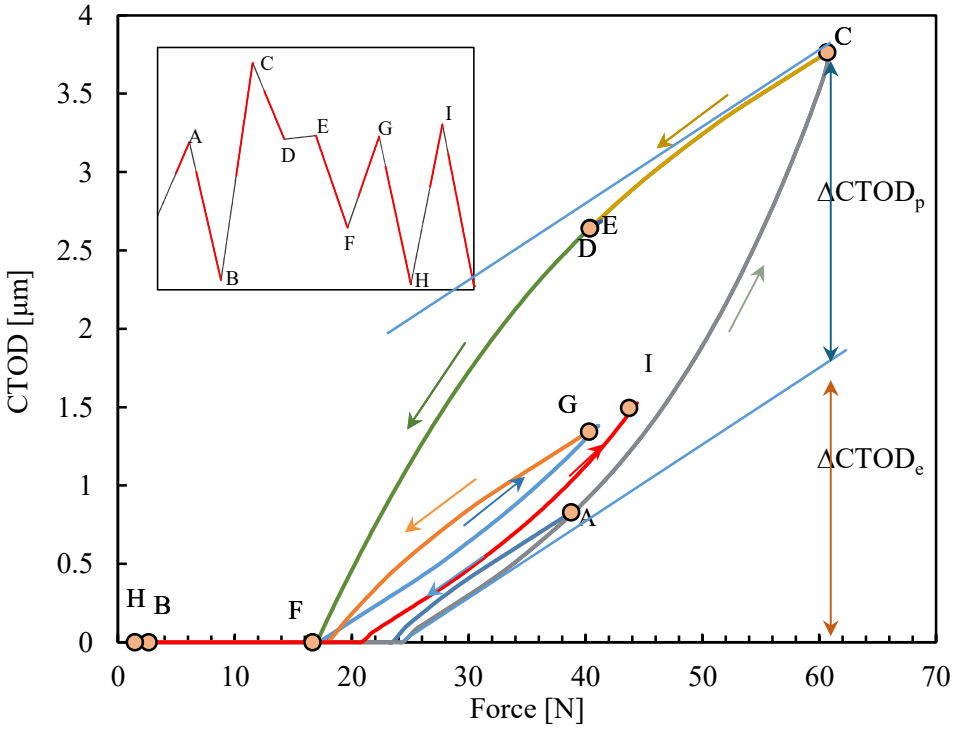

Figure 4.4 CTOD curve evaluated for a=15.8 mm, 98th load block, from cycle 52 to cycle 56 of pattern A.

4.1.4. Crack closure level

The modified crack closure level quantifies the fraction of load cycle during which the crack is closed, and the modified crack open level determines the fraction of the load cycle that is open. Those parameters were evaluated during the load block for a crack length of 15.80 mm. The modified crack open level (U^*_{open}) is calculated using the following parameters:

$$U^*_{open} = \frac{F_{open} - F_{min}}{F_{max} - F_{min}} \times 100\%$$

where F_{open} is the crack opening load, F_{min} is the minimum load and F_{max} is the maximum load. The modified crack closure level ($U^*_{closure}$) it is determined by the following parameters:

$$U^*_{closure} = \frac{F_{closure} - F_{min}}{F_{max} - F_{min}} \times 100\%$$

where $F_{closure}$ is the crack closed load.

Figure 4.5 shows the modified crack closure level and the modified crack open level for part of the load block, there are cycles in which the crack is closed since U^*_{open} is 100 % and $U^*_{closure}$ is 100%. The applied force is not sufficient to open the crack, which is associated with small load amplitude cycles. So, in this case F_{open} will be higher than F_{max}, but for convenience the values of U^*_{open} and $U^*_{closure}$ have been arbitrarily set to 100%. This coincides with the results of the Figure 4.2, since there is no plastic strain in small amplitude cycles.

When the crack is open, U^*_{open} and $U^*_{closure}$ are typically between 50% and 80%. These values are high, indicating that most of the load cycles are in the elastic range. (Figure 4.6). In the overload region, the values U^*_{open} and $U^*_{closure}$ are lower than the other cycles. The crack tends to open when a force of about 8 N is applied, as the amplitude of the loading cycle is much higher than the remaining cycles, the fraction of the cycle that is in the elastic range is lower than the remaining cycles.

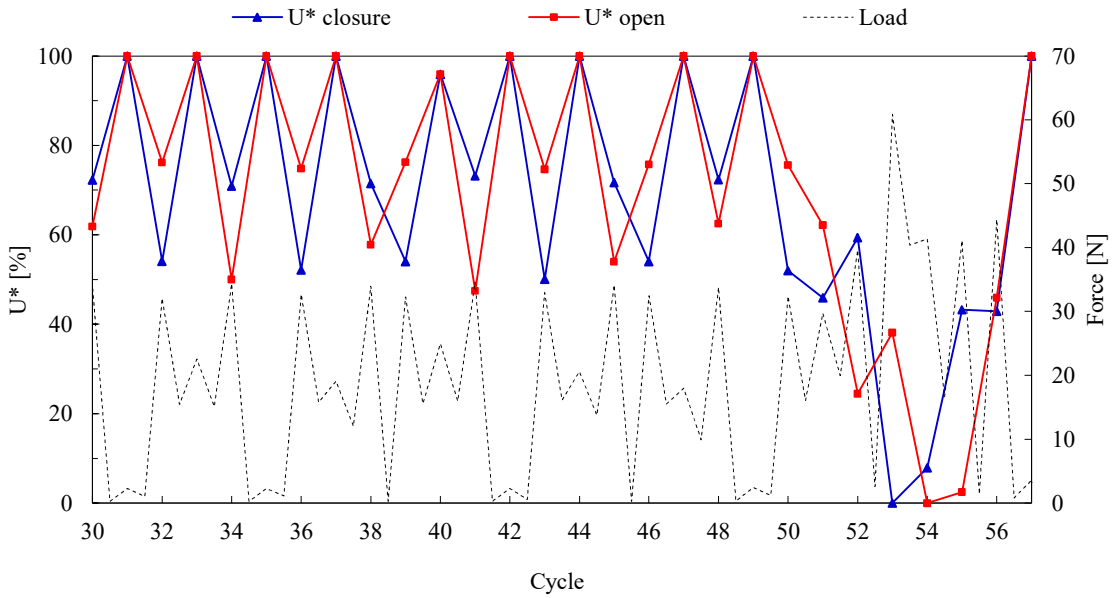

Figure 4.5 Modified crack closure level and crack open lever, in the 98th load block (a0=15.8 mm), between 40th and 57th cycle.

In addition to the previous findings, it was observed that the force values for crack closure and opening remain nearly constant throughout the loading block (Figure 4.6), except during the overload. Due to crack tip blunting, the force value to open the crack after an overload (17,2 N) is significantly lower than values for the rest of the cycles, it is noticeable also in Figure 4.4. This blunting effect reduces the force value to open the crack in the subsequent cycles, therefore increasing the level of plastic deformation produced. The damaging effect of the load cycles following the overload is partly explained by the blunting produced by the overload.

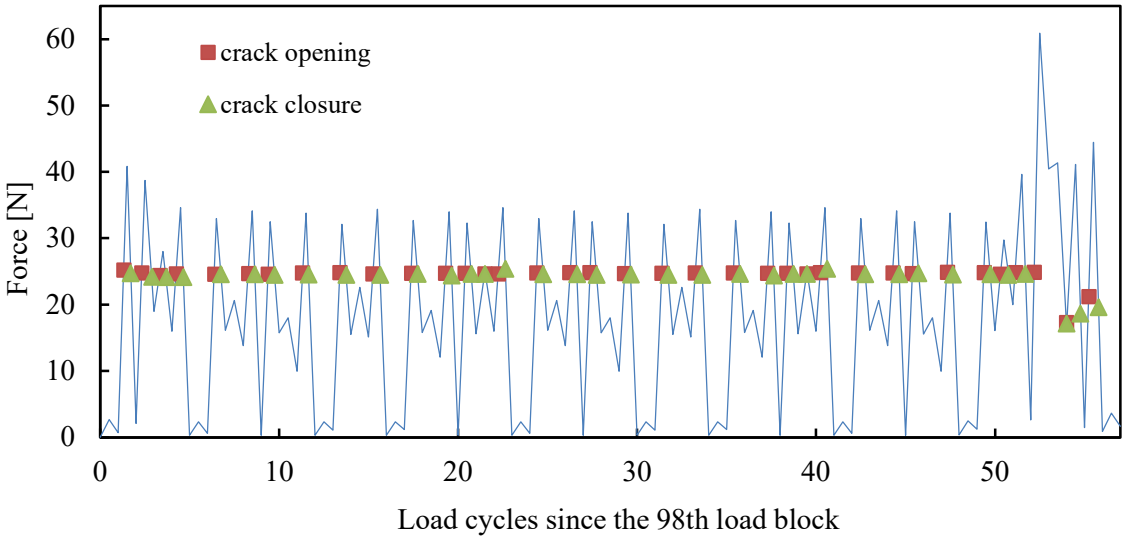

Figure 4.6 Force values for crack closure and crack opening for pattern A.

4.2. Variable amplitude without contact for pattern A

To evaluate the effect of the crack closure on FGC, the crack growth for pattern A is compared to the same pattern under the hypothetical condition where there is no contact between the crack flanks of the CT specimen. This simulates a case in which crack closure is not considered. The results of the FCG for both cases are presented in Figure 4.7. Accordingly, Figure 4.7(a) shows the evolution of crack length after every load cycle. Figure 4.7(b) presents the variations of crack growth rate per cycle (da/dN) with the current crack size, varying for both cases. The number of load cycles required for the VAL with contact between the crack flanks to reach a crack length of 15.80 mm is 5589 load cycles, equivalent to 98 load blocks. Without the presence of crack flanks, 567 load cycles and 10 load blocks are required to reach the same crack size. The result of this pattern supports the idea that plasticity-induced crack closure has an important effect on crack growth since the crack propagation rate is much faster without crack closure.

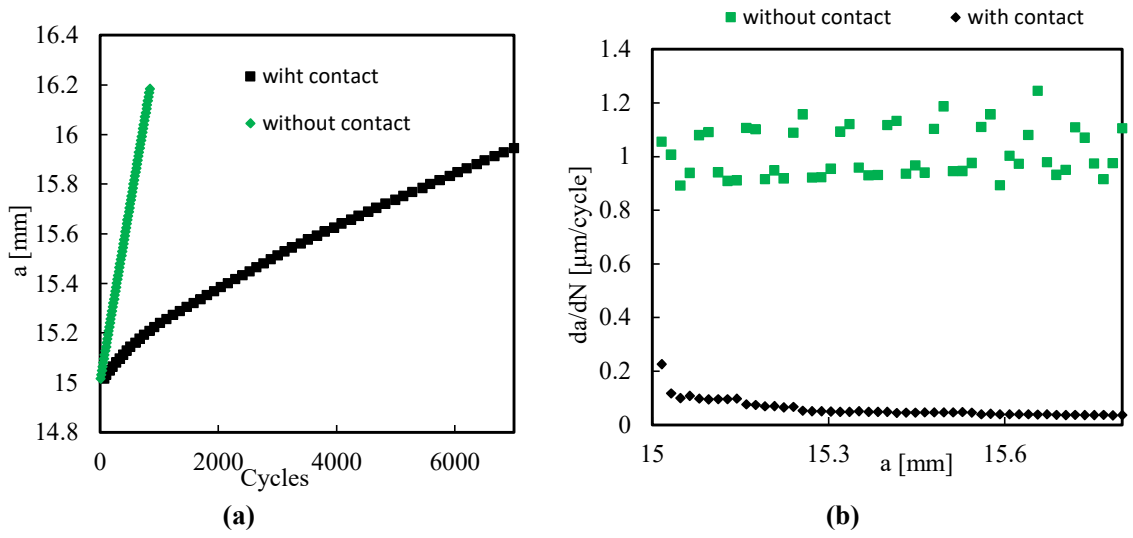

Figure 4.7 Comparison of the crack grow with and without contact between the crack flanks for the pattern A considering: (a) crack length per cycle; (b) da/dN versus crack length.

Figure 4.8 presents the evolution of plastic strain through a load block for the two cases presented before. The specimen with contact has no propagation during a load block, since the cumulative plastic strain does not reach 1.10, which is the critical value for crack propagation. In contrast, the specimen without contact has three node releases during the same load block. In the last part of the load block, crack propagation occurs more quickly due to the overload zone. Note that the cumulative plastic strain often exceeds 1.10, because

the crack propagation is only made at the minimum load. More than 40 cycles are required for two propagations to take place in the absence of contact, while the 3rd propagation in this block takes place after 11 cycles. This is an effect of the existence of a zone of overload in this part of the block.

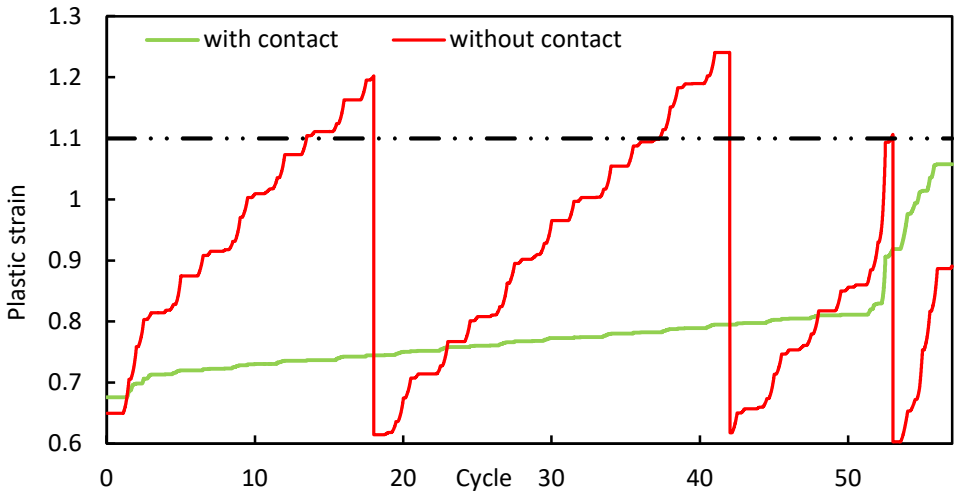

Figure 4.8 Comparison of plastic strain between specimens with contact and without contact for a=15.80 mm in pattern A.

The CTOD plots obtained without contact between the crack flanks are present in Figure 4.9. Note that a negative value is obtained, indicating an overlap of the crack flanks at the minimum loading force, which cannot occur in a physical specimen. The crack tends to open immediately from the minimum loading force, contrary to what happens in Figure 4.4, in which the contact between the crack flanks is considered. In any case, the shapes of the CTOD curves are identical to the curves obtained with contact. The CTOD for the non-contact simulation is almost twice the CTOD for the contact simulation in the overload zone. This results in a faster evolution of the crack growth, which explains the differences in the FCG of Figure 4.7.

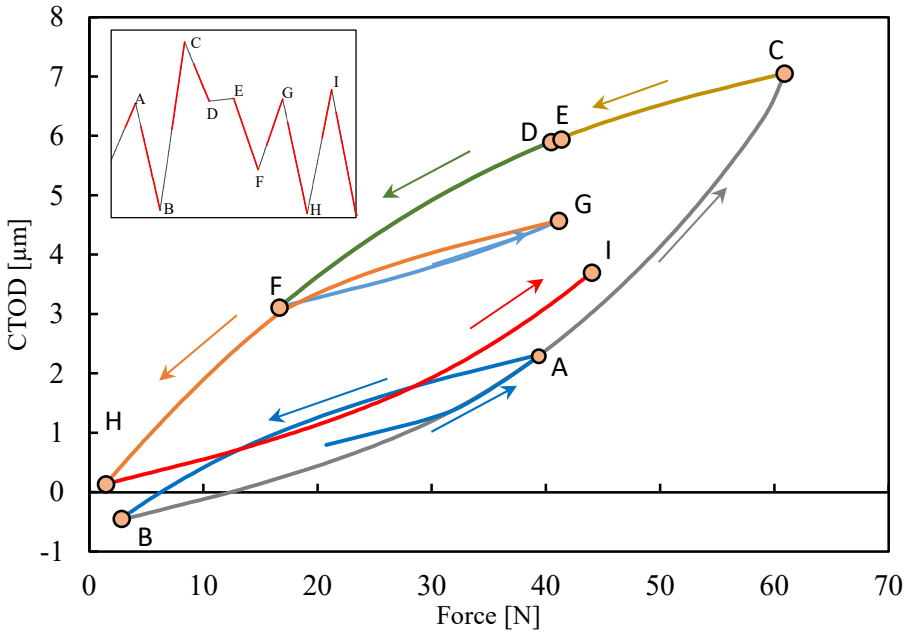

Figure 4.9 CTOD curve evaluated for a=15.8 mm from cycle 52 to cycle 56 of 130th block, without contact on the flank for pattern A.

4.3. Constant amplitude loading for pattern A

To explore the possibility of a simplification in the analysis of complex loadings, the VA loadings are compared to Constant Amplitude Loadings (CAL) to observe if there are any correlation between the two types of loadings for this study. The work of Aursand *et al*. [63] on mooring line steel under variable amplitude loading will be considered in this study.

Under variable amplitude loading, a commonly used engineering method for fatigue life estimation is the Miner rule [73]. To transform pattern A into a CAL, it was necessary to define the mean load value for all points in the spectrum, P_{mean}. Assuming no sequence effects, implying that the Miner rule is valid [73], a hypothesis for equivalent load range could be as follows:

$$\Delta P_{eq} = \sqrt[3]{\frac{1}{n}\sum_{n} |\Delta P_i|^3} \tag{4.1}$$

Using ΔP_{eq}, the minimum (P_{min}) and maximum (P_{max}) force could be determined as follows:

$$P_{min} = P_{mean} - 0.5 \times \Delta P_{eq} \quad (4.2)$$

$$P_{max} = P_{mean} + 0.5 \times \Delta P_{eq} \quad (4.3)$$

The load spectrum of the CAL is shown in the Figure 4.10. P_{max} is 29.95 N, P_{min} is 4.85 N and P_{mean} is 17.40 N. The amplitude is constant throughout the spectrum and plastic zones are also constant from cycle to cycle.

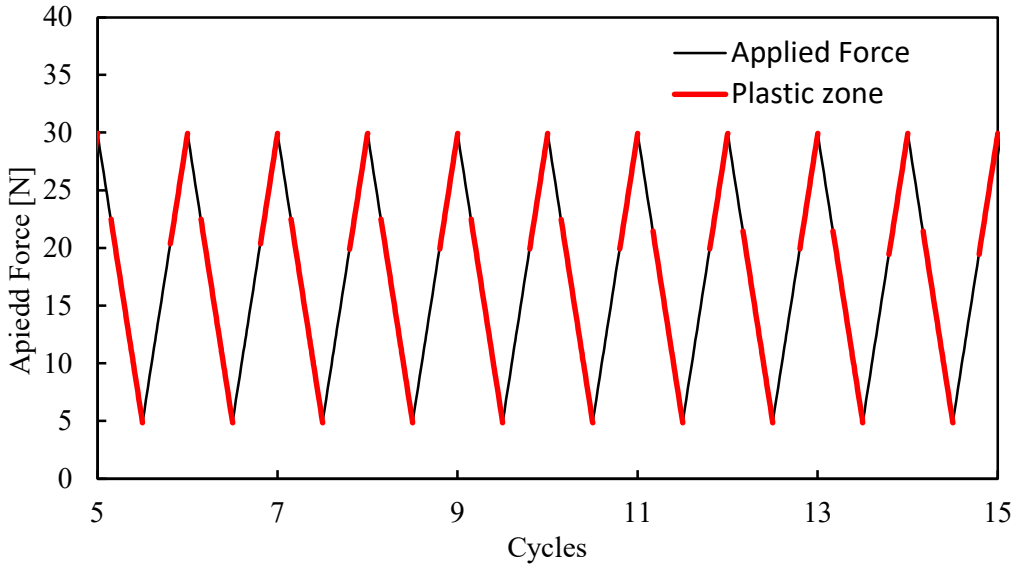

Figure 4.10 Constant Amplitude Loading derivate from Pattern A.

Figure 4.11 presents the CTOD for a cycle after a node release of the CAL pattern. It also indicates the crack opening force and the crack closing force. In each cycle, the crack opens at a force lower than pattern A, as shown in the Figure 4.11. The plastic domain starts at the force of 21 N for loading. During unloading, the elastic region has a range of approximately 7.5 N and then plastic deformation starts. Note that in each cycle the crack opens at a force higher than the force for closing the crack, as shown in the CTOD plot, Figure 4.11.

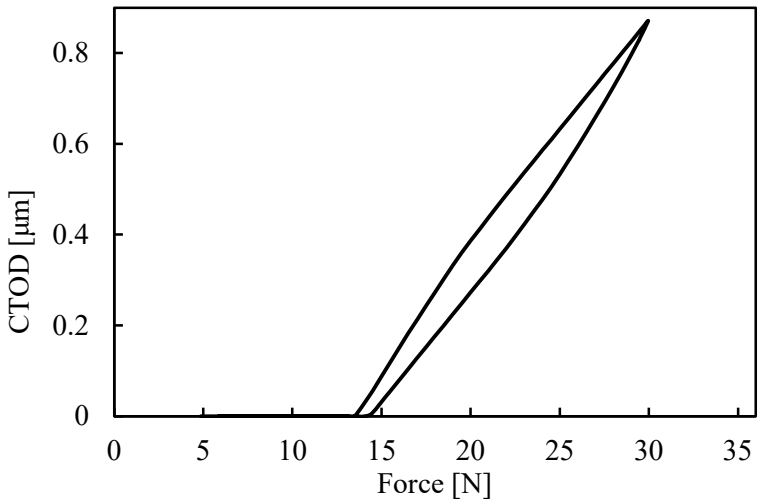

Figure 4.11 CTOD for the CAL transformed form pattern A and a=15.80 mm.

Figure 4.12 compares the FCG rate of the pattern A and the CAL transformed from pattern A. In both cases the FCG rate decreases up to a crack length of 15.10 mm. Thereafter, the FCG rate tends to increase for the CAL, which is associated with a stable crack propagation zone. For the crack length of 15.80 mm, the FCG rate for CAL is almost twice the FCG ratio for pattern A.

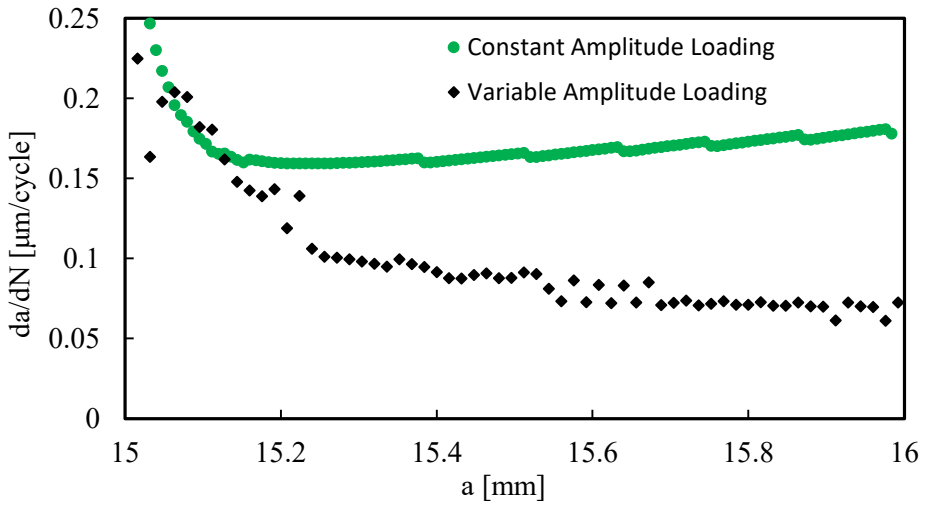

Figure 4.12 Comparison of FCG ratio between pattern A and a CAL derivate from pattern A.

4.4. Load Pattern B

4.4.1. Fatigue crack growth rate

Figure 4.13 presents the evolution of the variations of crack growth rate per loading cycle (*da/dN*), with the current crack size of 15 mm for the respective load pattern B.

Comparing this load pattern with pattern A, the variation of FCG over the cycles is not as abrupt. FCG rate decreases up to a=15.40 mm and then stable crack propagation is achieved, linked to the second region of the da/dN–ΔK curve (Figure 2.1) [2]. After achieving a crack length of 15.40 mm, FCG tends to increase, which is explained by the increase of crack tip stresses with crack length. At a crack length of 15.80 mm, the FCG ratio is close to the FCG rate obtained for pattern A.

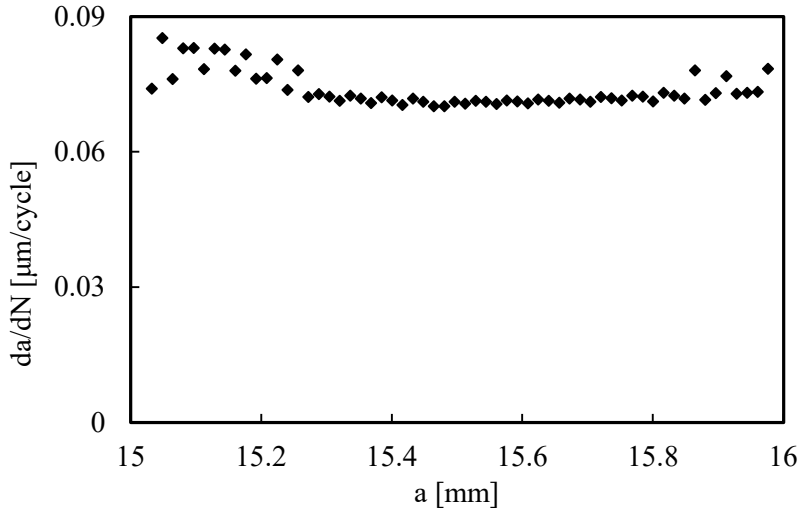

Figure 4.13 Fatigue crack growth rate versus the crack length for the pattern B.

4.4.2. Plastic strain in a load block

The load block shown in Figure 3.3 was repeated several times. It took 130 load blocks to reach the crack size of 15.80 mm. The cycles between the 60th and the 85th are shown in Figure 4.14. In this load block there are cycles with a high amplitude load, such as cycle 65, and cycles with a low amplitude load, as an example of cycle 80.

The block consists of an irregular pattern of high amplitude cycles combined with a series of low amplitude cycles. For this load block, the plastic strain value in cycle 60 is 0.61. It continues to increase throughout the block until reaching 0.79 at the end of the 85th cycle. (Figure 4.14). There is no node propagation between 60th and 85th cycles.

Figure 4.14 shows that the increase in the cumulative strain takes place during loading and unloading, as indicated by the blue segments. For example, in cycle 65, the increase of plastic strain during the loading phase is the same magnitude as the increase of plastic strain during the unloading phase. There is no overload zone in this pattern, so the plastic strain does not increase significantly in a specific part of the pattern in contrast to pattern A. For the small amplitude cycles, there is no plastic deformation in the cycle and the cumulative plastic strain remains constant.

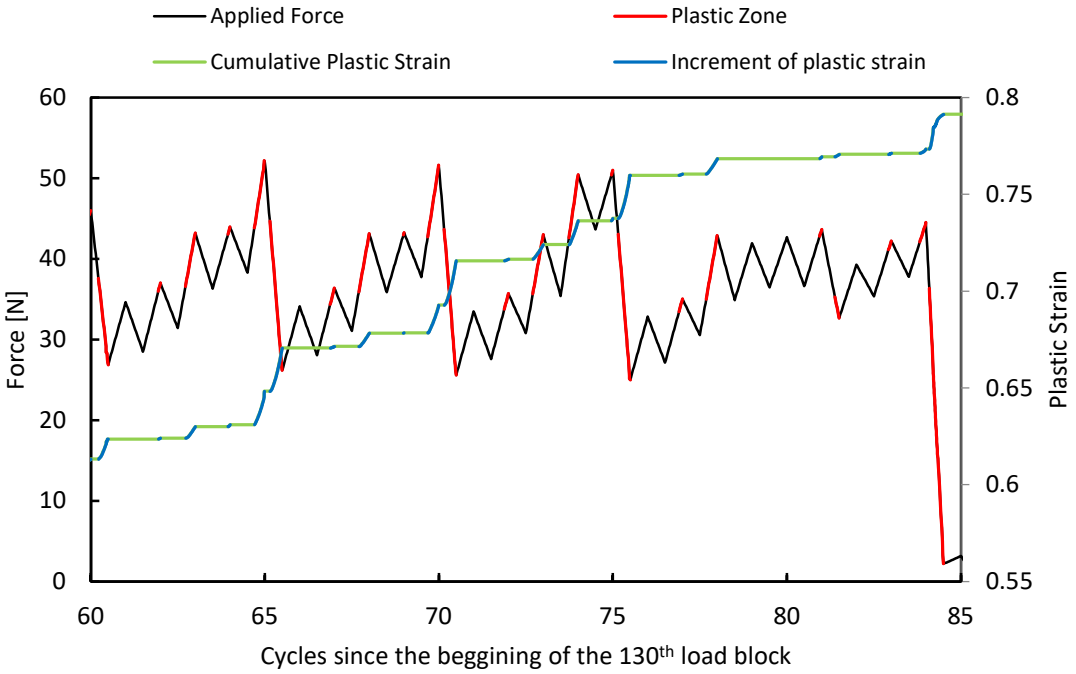

Figure 4.14 Cumulative plastic strain and plastic zones in a load block for pattern B.

4.4.3. CTOD of pattern B

The CTOD analysis was carried out for pattern B. Five cycles of the 130th load block was analysed. Accordingly, cycles 61 to 65 are shown in the Figure 4.15, indicated by the letters A to K. This sequence, which is repeated through pattern B and is characterised by low amplitude cycles, with the applied force increasing from cycle to cycle, followed by a higher loading and unloading amplitude cycle at the end of the sequence. The analysis of CTOD for this group of cycles may readily provide an understanding of other parts of pattern B.

In this group of cycles, plastic strain occurs in the loading phase close to the peak and in the unloading phase with the highest amplitude loading, from J to K.

The CTOD values do not exceed 1.7 and are very distant from the CTOD values of the overload zone for pattern A (Figure 4.4). The maximum force is also lower and does not reach 52 N. In Figure 4.15 one may just observe one big loop, in contrast from what happens in pattern A.

In the first three load cycles, the points below 36 N are in the elastic region and no plastic deformation occurs below this force. The elastic region is represented by the straight lines ($\Delta CTOD_e$) in the CTOD curve. During unloading from F to G and H to I there is no

plastic deformation, this is represented by straight segments in the CTOD curve. During unloading from J to K, plastic deformation occurs only after a period of the elastic region. The elastic region is also the straight part of the segment parallel to the green line. Even this high amplitude unloading (from 52 N to 26N), is not sufficient to close the crack and the CTOD for point K is not zero. Note that during the loading phase from I to J, plastic strain occurs after a period of elastic domain. Near the point with the force of 44 N (point with the same magnitude of H) the plastic strain starts, and it is visible that the straight line turns into a curve. Observe that at point J the CTOD is 1.70, however most of this opening is elastic, because $\Delta CTOD_e$ is greater than $\Delta CTOD_p$. differently from what happens in pattern A (Figure 4.4) where $\Delta CTOD_e$ and $\Delta CTOD_p$ had approximately the same magnitude.

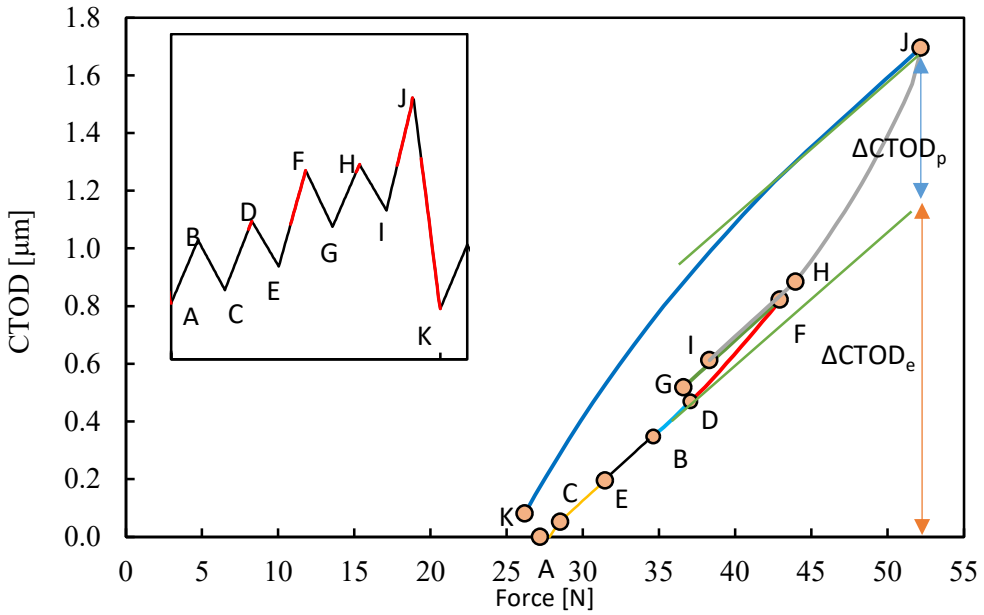

Figure 4.15 CTOD curve evaluated for a=15.8 mm, 130th load block, from cycle 61 to cycle 65 of pattern B.

4.4.4. Crack closure level

Figure 4.16 shows the relation between $U^*_{closure}$ and U^*_{open} with the applied force in some cycles of pattern B. The CTOD values in Figure 4.15 are higher than zero for most of the cycles, indicating that the crack is often open. It is also noticeable in the Figure 4.16 that for most of the cycles the values of $U^*_{closure}$ are 0% and U^*_{open} are 0%, indicating that the crack is open. The cracks tend to close after the high amplitude unloading phases (example from cycle 43). Then, the crack opens again during the next loading phase and remains open until the next high amplitude unloading phase.

The Figure 4.17 shows that the force typically applied for crack propagation is higher for pattern B than for pattern A (Figure 4.6). The force applied to close the crack is also

greater than that applied for pattern A. The range of applied force remains between 30 N and 50 N, higher than the magnitude of the force applied in pattern A. This results in lower values of U^*_{open} and $U^*_{closure}$ relative to pattern A because the crack tends to open or close for values of force close to F_{min}, however F_{min} for cycles of Pattern B is higher than F_{min} for cycles of Pattern A. Note that during the part of pattern B shown in Figure 4.16, only in one cycle the value of U^*_{open} and $U^*_{closure}$ exceeds 50%.

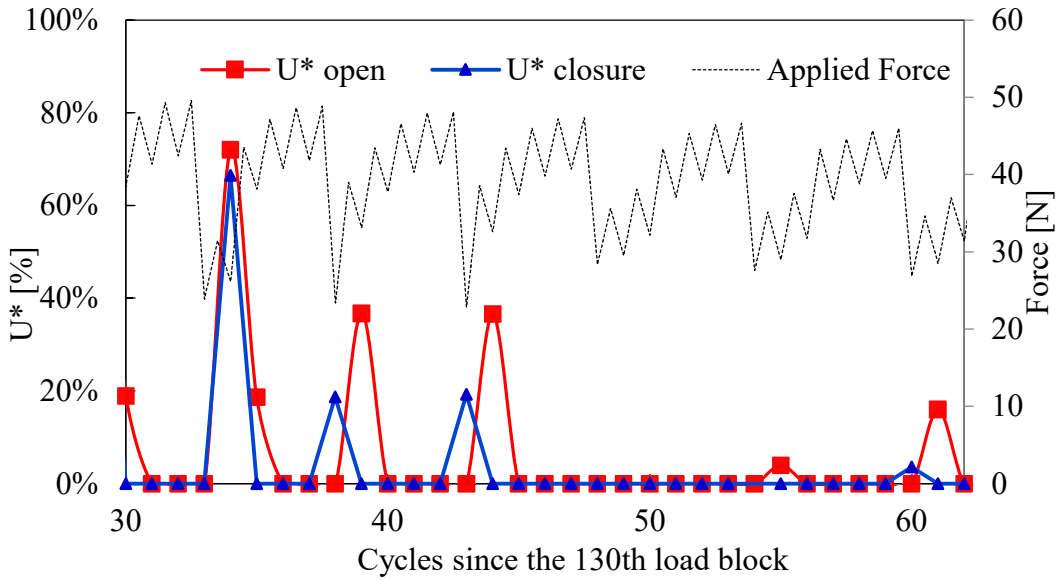

Figure 4.16 Modified crack closure level and crack open lever, in the 130th load block (a_0=15.8 mm), between 30th and 62nd cycle.

During this load block, the opening force tends to decrease in the same way as the closing force, showing very close values throughout the block and following the same downward trends as shown in Figure 4.17. After a high amplitude load as it occurs in Cycle 1 and 2, the force for the next crack opening is lower than the remaining cycles due to the blunting effect.

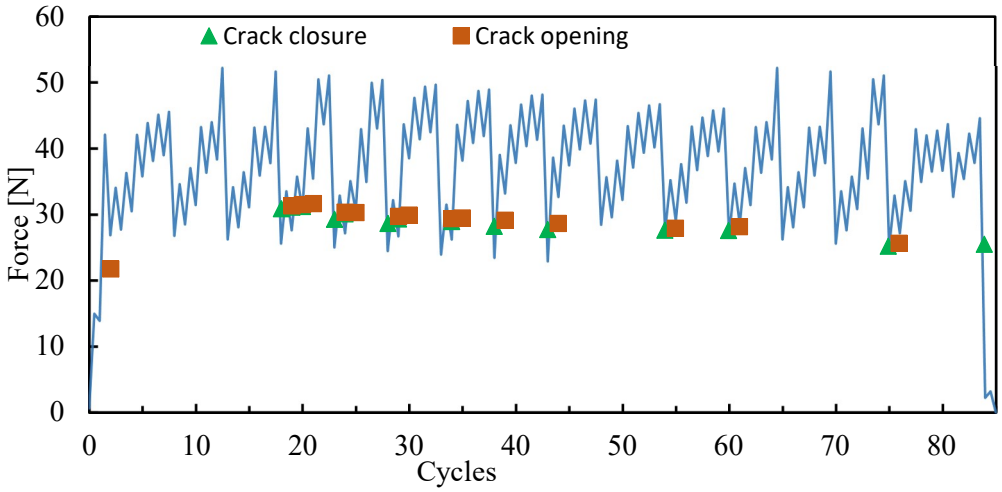

Figure 4.17 Force values for crack closure and crack opening for pattern B.

4.5. Variable amplitude without contact for pattern B

To understand the crack closure phenomenon in a different pattern, without an overload zone, the study without contact between the flanks of the CT specimen was carried out on pattern B. The two blocks studied, one with contact and the other without contact had a crack length of 15.80 mm. This corresponds to the 91st block without contact and the 130th for the simulation with contact between the flanks. The first parameter to be compared was the FCG rate. To achieve a crack length of 15.80 mm, 10990 load cycles were required in the contact simulation and 8015 cycles in the non-contact simulation. Figure 4.18 shows that the difference in FCG between the two simulations for this pattern is smaller than the difference in FCG rate between the contact and non-contact simulations for pattern A.

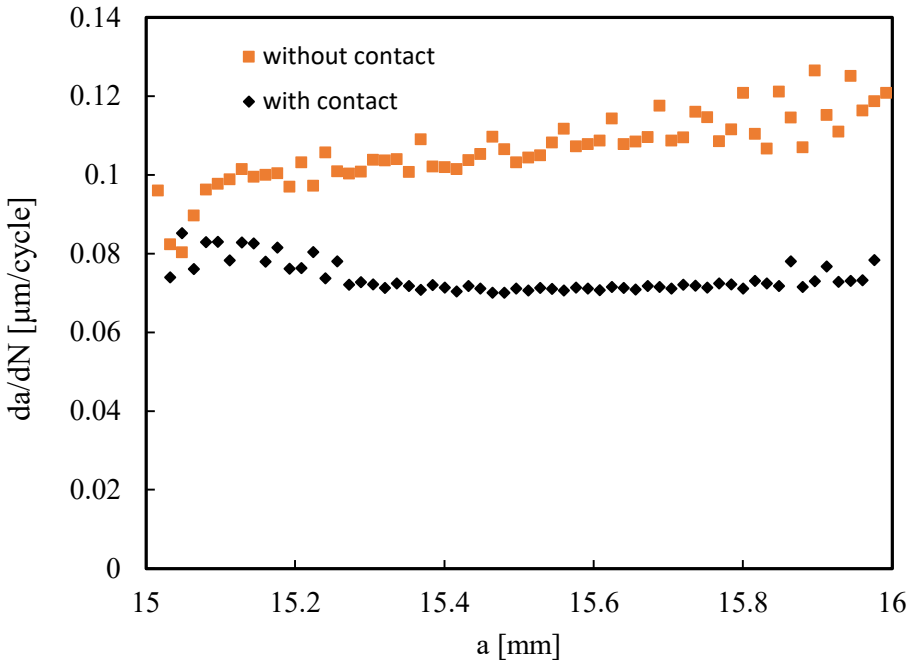

Figure 4.18 Comparison of the FCG with and without contact between the crack flanks for the pattern B.

The evolution of plastic strain for both simulations is illustrated in Figure 4.19. In both cases there is one node propagation in the middle of the block. Both cases present a similar increase of plastic strain (slope of the curves). Even the plastic strain rate is the same, although in the case without contact, FCG rate is higher. This is because of the plastic strain after node propagation. For the non-contact specimen, the plastic strain after a propagation has a value of around 0.5, while the plastic strain for the case with contact between the flanks is approximately 0.4. These initial values result from the accumulation of plastic strain before the crack tip reaches this position. The difference between these values is due to the unequal stress distribution ahead of the crack tip, where the flanks are in contact. To reach a plastic strain of 1.10 and for the node to propagate, it takes more cycles in the simulation with contact between the flanks. This explains the reason behind the higher value of FCG rate in the simulation without contact, in Figure 4.18.

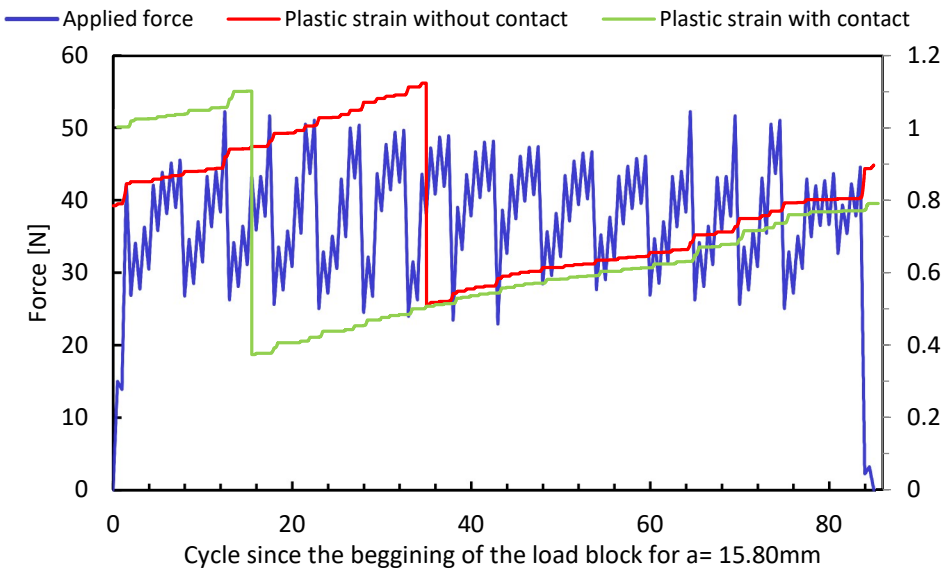

Figure 4.19 Comparison of plastic strain between specimens with contact and without contact between the flanks for a=15.80 mm in pattern B.

Figure 4.20 shows the CTOD plot for three cycles of pattern B without contact between the flanks. The shape of the plot is similar to the plot with contact between the flanks. As it was observed in pattern A, the value maximum of CTOD is much higher in the case where there is no contact between the flanks.

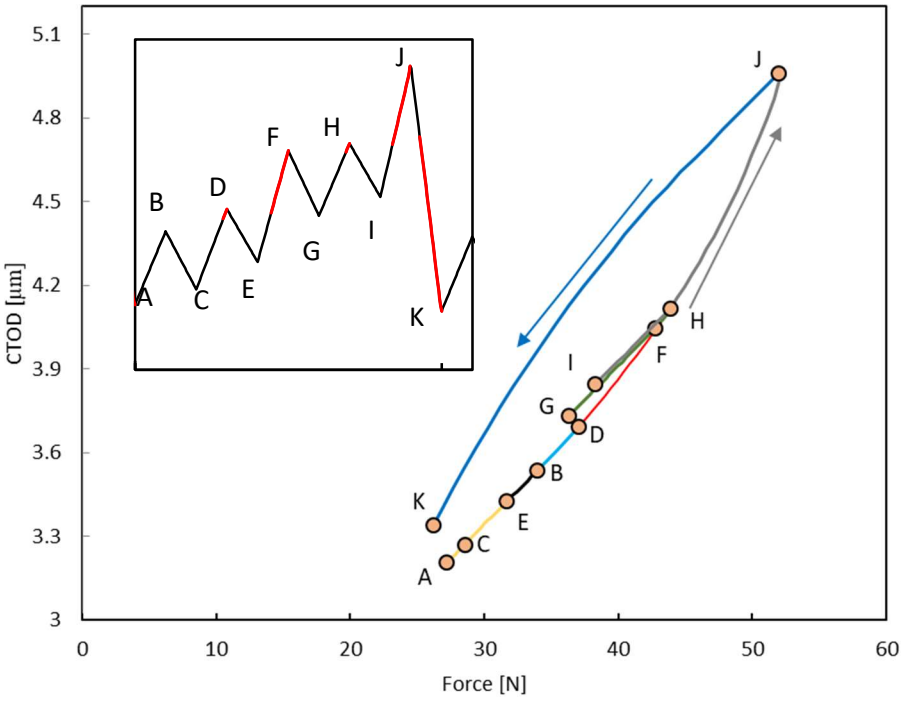

Figure 4.20 CTOD curve evaluated for a=15.8 mm from cycle 61 to cycle 65 of 91st block, without contact on the flank for pattern B.

4.6. Constant amplitude loading for pattern B

The transformation of a CAL pattern was carried out for pattern B, as it shows in Figure 4.21. The procedure for the transformation was the same as the one that was used for the pattern A. P_{max} is 43.45 N, P_{min} is 30.09 N and P_{mean} is 36.77 N.

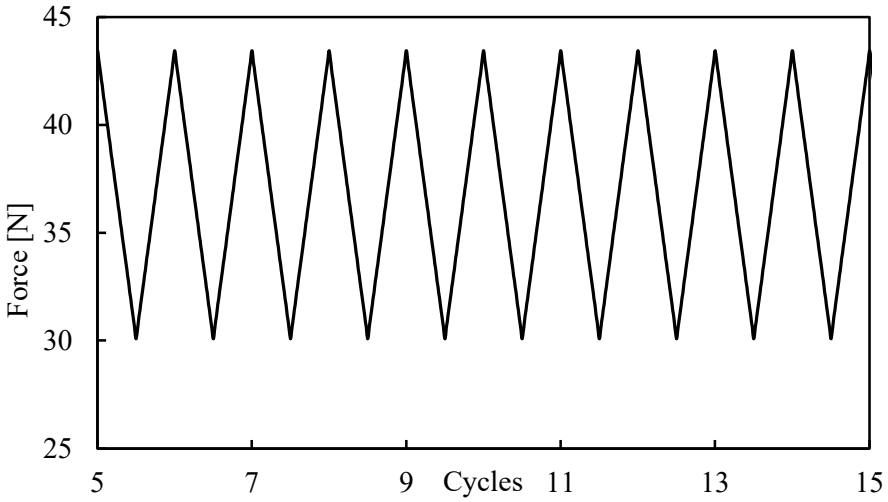

Figure 4.21 Constant Amplitude Loading of the Pattern B.

Figure 4.22 shows the FCG evolution of pattern B and pattern CAL derived from pattern B. In the CAL pattern the FCG ratio increases with the crack length, whereas in the VAL pattern the FCG ratio remains constant over the cycles. Nevertheless, the VAL pattern has a higher FCG ratio than the CAL pattern. CAL has a lower FCG ratio because pattern VAL B has some load cycles with high amplitude variation, whereas the CAL derived from pattern B has only 13.36 N of amplitude variation, with more than 7.5 N of the load cycle belonging to the elastic regime.

This contrasts with pattern A, where the CAL pattern has a higher FCG ratio than the VAL pattern. The reason for this is that the CAL for Pattern A has a higher amplitude in all load cycles, approximately 25.1 N. This means that the complex loads cannot be simplified using the Miner rule.

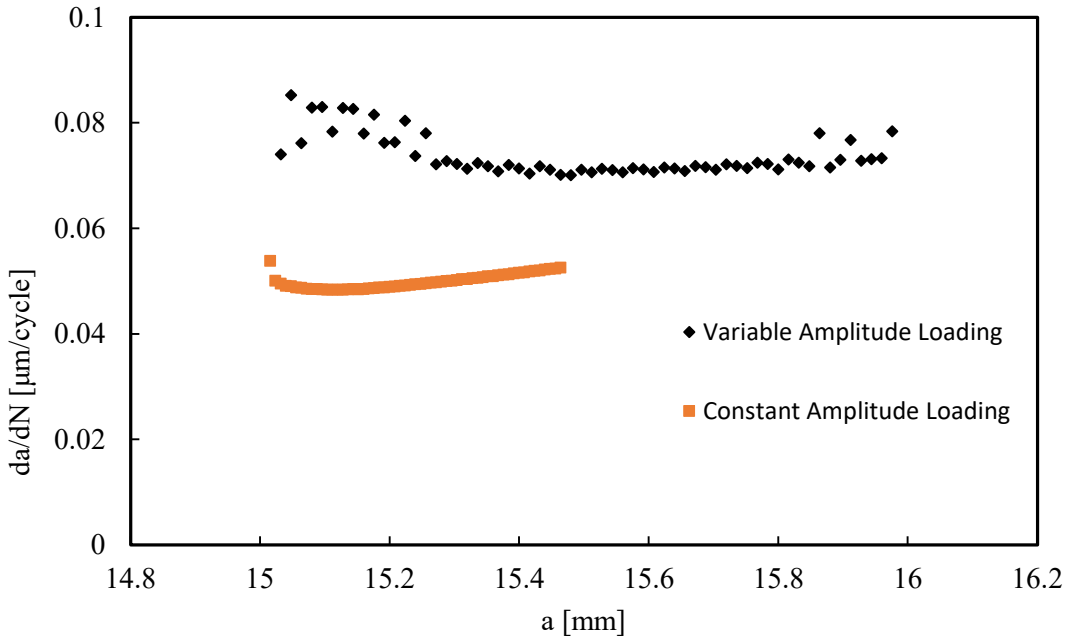

Figure 4.22 Comparison of FCG ratio between pattern B and a CAL.

5. DISCUSSION OF RESULTS

5.1. Omission of the small cycles

5.1.1. Limit of elastic zone

To determine the range of the elastic zone during the load cycles, patterns A and B are analysed. This analysis considers the points during the unloading phase and considers the points that start in the plastic domain at the peak, enter the elastic domain during unloading and then return to the plastic strain as shown in the Figure 5.1.

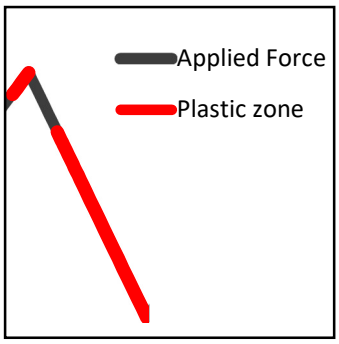

Figure 5.1 Unloading phases considered to determine the elastic range.

The elastic limit intensity factor (ΔK_{lim_elas}) of each load cycle for the two load patterns, as a function of the maximum force applied in a load cycle, is shown in Figure 5.2 The squares represent this data for a load block in pattern A, while the triangles represent analogous data for a load block of pattern B. The results show that plastic deformation occurs for ΔK values greater than 3.20 MPa.m$^{0.5}$.

The limit of elastic regime may be compared with the fatigue threshold obtained in conventional FCG tests [74], [75]. Note that ΔK_{lim_elas} is almost twice the crack propagation threshold. This difference in values may be related to the fact that numerical simulation does not consider some environmental factors that are responsible for crack closure and slow down the FCG as in the case of OICC [76]. The value of ΔK_{lim_elas} is almost constant in a graph.

For this CT specimen a value of ΔK_{eff} 3.20 MPa.m$^{0.5}$ corresponds to a loading force of 7.50 N. This analysis reveals that the plastic region is not reached during the unloading phase if the load cycle amplitude is lower than 7.50 N. The conclusion can be drawn that ΔK_{eff} is

independent of K_{max} [5], since for different values of F_{max} the values of ΔK_{lim_elas} remain in the same range.

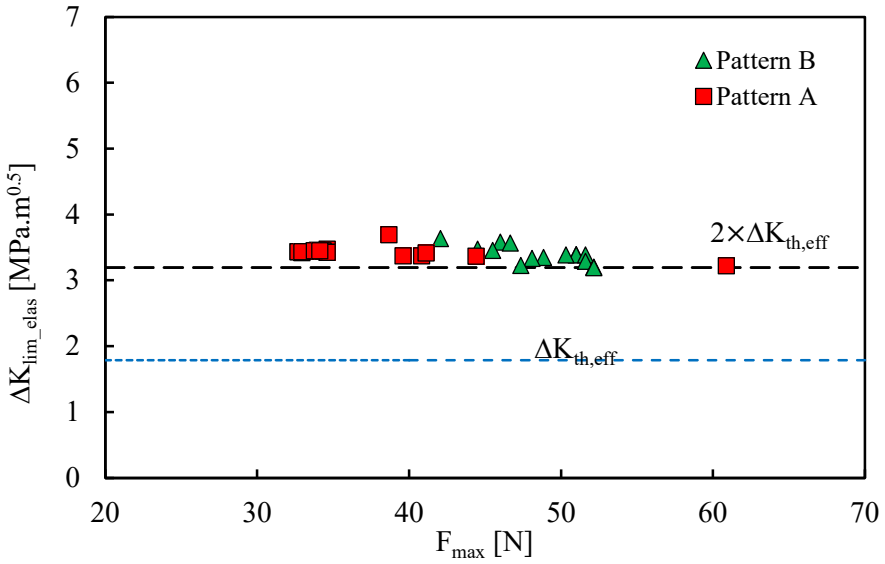

Figure 5.2 Limit of K elastic range versus maximum load per cycle for a load block of pattern A and B with a=15.80mm.

5.1.2. Pattern with omission of cycles

To determine whether the presence of small cycles where no plastic deformation occurs influences FGC, pattern A was studied but excluding cycles without plastic deformation. Figure 5.3 shows the procedure for omitting small cycles. If the amplitude of the cycles from B to C is lower than the value of ΔK_{lim_elast} the load cycle is omitted. Figure 5.3(a) shows the loading phase omitting the elastic domain cycle and considering only points A, B, D' instead of points A, B, C, D. The same procedure has been used for the unloading phases (Figure 5.3b).

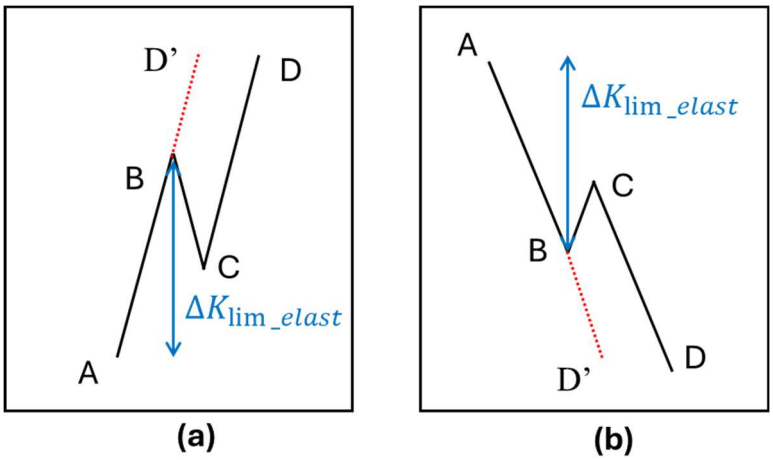

Figure 5.3 Representation of the cycles omitted. (a) during loading phase. (b) during unloading phase.

Figure 5.4 shows the pattern A with the elastic cycles omitted. The graph is similar to that of pattern A, but the number of cycles in the pattern has been reduced from 57 to 32. This pattern still has the overload zone.

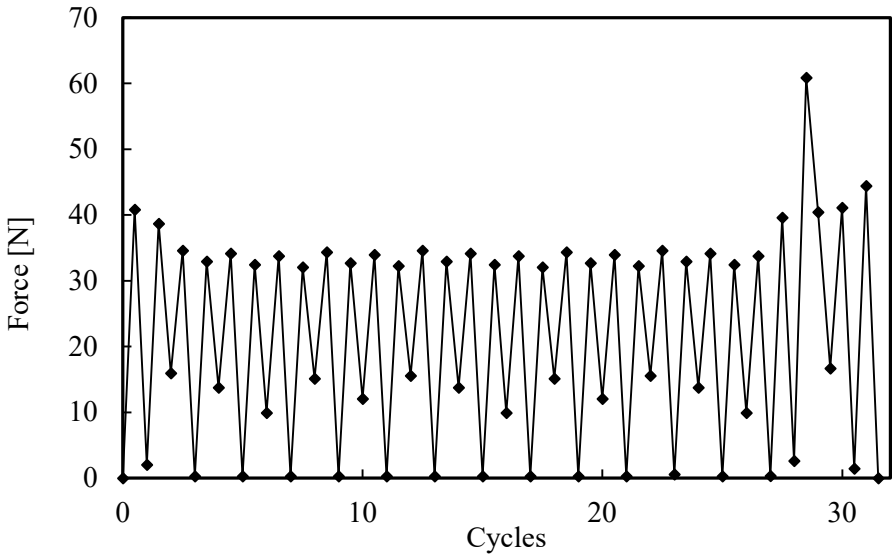

Figure 5.4 Pattern A with the omission of cycles.

5.1.3. Effect of the omission of cycles

FCG was compared for pattern A with and without cycle omission and is shown in Figure 5.4. The comparison is made in μm per load block as the two load patterns have a different number of cycles, 57 load cycles for pattern A and 32 for pattern where cycles are

omitted. Figure 5.5 shows that the FCG per load block is almost the same for each pattern. This is an indication that the cycles in the elastic region have no effect on crack propagation.

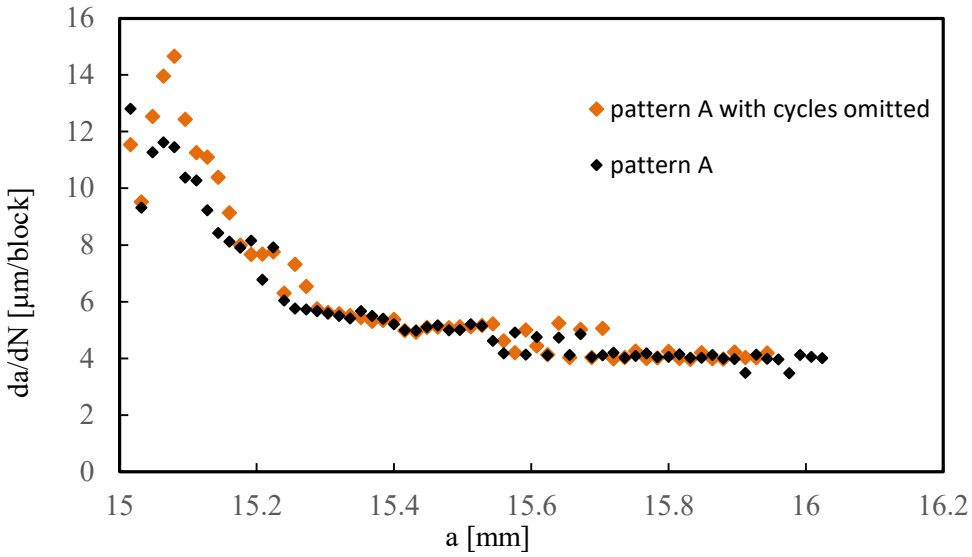

Figure 5.5 FCG ratio per load block of patter A with and without omission of load cycles.

5.2. Crack closure mechanism

Pattern A shows an FCG ratio that is 10 times higher for the load without contact between the flanks than for the load with contact between the flanks. In pattern B, the difference is less than double. The effect of the elimination of the contact is greater in the case of pattern A than in the case of pattern B. This means that the crack closure mechanism has a greater influence in the case of pattern A. Defining a load ratio for a VAL is very difficult. However, the stress ratio in pattern A is lower than in pattern B if the difference between F_{max} and F_{min} is more significant in pattern A. Pattern A has some peaks of force higher than 35 N and some valleys of 5 N, whereas in pattern B the force is higher than 25 N and lower than 50 N for most of the cycles. The effect of the elimination of the contact between the flanks is more expressive in pattern A, from which it can be deduced that the crack closure phenomenon is more significant in models with lower stress ratios.

6. CONCLUSIONS

In this thesis, a study of the effect of variable amplitude loading in FCG was carried out. Two different patterns were analysed. These patterns were derived from two train loads on a railway bridge. Cumulative plastic deformation at the crack tip was considered the driving force for FCG in the numerical model. Some important conclusions can be drawn from the numerical results obtained.

- The overload zone is the main factor responsible for the increase in plastic strain. Pattern A has an overload during the load block. The analysis of the cumulative plastic strain in this pattern shows that 75% of the increase in plastic strain during the block occurs during the overload cycles. In Pattern B, the increase in plastic strain is almost constant throughout the block, which is consistent with the absence of overload zones during this pattern.
- Elastic cycles, where there is no plastic deformation, can be omitted. Pattern A was compared with a pattern where the elastic cycles were not considered. The results of the FCG per load block are identical in the two simulations. The time and memory requirements for numerical simulations can be reduced by this simplification.
- The validity of Miner's law was investigated for two load patterns. The correlations of FCG between VAL and CAL were very different in both cases and from the original article, leading to the conclusion that Miner's law cannot be applied to all complex load patterns.
- The effect of crack closure is important in low stress ratio patterns and has less influence in high stress ratio patterns. The pattern A has a low value of stress ratio and showed a high difference of the FCG rate between the numerical simulations with and without the contact between the flanks of the CT specimen. On the other hand, pattern B has a high value of stress ratio and the differences in FCG rate were less significant.
- The amplitude of the load is the most important factor for the crack closure and the maximum force of the cycle has no influence on the crack closure. Each cycle of the two load patterns has been studied and the conclusion has been

reached that for this material and numerical model, a load amplitude of 8N (respectively 3.2 MPa.m$^{0.5}$) during the unloading phase will be required for the cycle to enter the plastic domain and initiate plastic deformation. The amplitude of the elasticity is still constant for cycles with different maximum forces.

- This study does not consider the weight of the bridge, which had some different results in the study of the real load case, caused by the increase in tensions in the railways.

Following this thesis, it is important to analyse other real load patterns to compare with the two patterns studied in this thesis. Namely, to extend the omission of the theory of elastic cycles, which is very important for the studied of fatigue, once that can minimise cost and time. The comparison of numerical predictions with experimental results obtained for the same loading patterns will also be important for the validation of the numerical models.

REFERENCES

[1] U. Zerbst, M. Vormwald, C. Andersch, K. Mädler, and M. Pfuff, 'The development of a damage tolerance concept for railway components and its demonstration for a railway axle', *Eng Fract Mech*, vol. 72, no. 2, pp. 209–239, Jan. 2005, doi: 10.1016/J.ENGFRACMECH.2003.11.011.

[2] P. Paris and F. Erdogan, 'A Critical Analysis of Crack Propagation Laws', *Journal of Basic Engineering*, vol. 85, no. 4, pp. 528–533, Dec. 1963, doi: 10.1115/1.3656900.

[3] F. Erdogan and M. Ratwani, 'Fatigue and fracture of cylindrical shells containing a circumferential crack', *International Journal of Fracture Mechanics*, vol. 6, no. 4, pp. 379–392, Dec. 1970, doi: 10.1007/BF00182626/METRICS.

[4] A. Hartman and J. Schijve, 'The effects of environment and load frequency on the crack propagation law for macro fatigue crack growth in aluminium alloys', *Eng Fract Mech*, vol. 1, no. 4, pp. 615–631, Apr. 1970, doi: 10.1016/0013-7944(70)90003-2.

[5] M. F. Borges, D. M. Neto, and F. V. Antunes, 'Revisiting Classical Issues of Fatigue Crack Growth Using a Non-Linear Approach', *Materials 2020, Vol. 13, Page 5544*, vol. 13, no. 23, p. 5544, Dec. 2020, doi: 10.3390/MA13235544.

[6] A. Micael Frias Borges Advisors, 'Effect of elasto-plastic properties on fatigue crack growth', 2021. Accessed: Jul. 05, 2024. [Online]. Available: https://estudogeral.uc.pt/handle/10316/93557

[7] D. M. Neto, M. F. Borges, F. V. Antunes, and J. Jesus, 'Mechanisms of fatigue crack growth in Ti-6Al-4V alloy subjected to single overloads', *Theoretical and Applied Fracture Mechanics*, vol. 114, p. 103024, Aug. 2021, doi: 10.1016/J.TAFMEC.2021.103024.

[8] D. M. Neto, E. R. Sérgio, M. F. Borges, L. P. Borrego, and F. V. Antunes, 'Effect of load blocks on fatigue crack growth', *Int J Fatigue*, vol. 162, p. 107001, Sep. 2022, doi: 10.1016/J.IJFATIGUE.2022.107001.

[9] D. M. Neto, E. R. Sérgio, F. Jesus, J. C. Newman, and F. V. Antunes, 'Fatigue Crack Propagation under Christmas Tree Load Pattern', *Applied Sciences (Switzerland)*, vol. 13, no. 3, Feb. 2023, doi: 10.3390/app13031284.

[10] D. M. Neto, M. F. Borges, F. V. Antunes, and R. Sunder, 'Numerical analysis of fatigue crack growth under SuperBlock2020 load sequence', *Eng Fract Mech*, vol. 260, p. 108178, Feb. 2022, doi: 10.1016/J.ENGFRACMECH.2021.108178.

[11] J. L. M. Tavares, 'Avaliação do Comportamento Estrutural de Pontes Ferroviárias Antigas com Base em Modelos de Acumulação de Dano', 2023. Accessed: Jul. 05, 2024. [Online]. Available: https://estudogeral.uc.pt/handle/10316/110731

[12] A. Silva Ribeiro, A. S. Ribeiro, utadpt José AFO Correia, A. L. L Silva, and A. M. P de Jesus, 'EVOLUTION OF FATIGUE HISTORY', 2010. [Online]. Available: https://www.researchgate.net/publication/299397997

[13] C. A. G. de Moura Branco, *Mecânica dos materiais*. 1998.

[14] G. R. Irwin, *Fracture BT - Elasticity and Plasticity / Elastizität und Plastizität*. Springer Berlin Heidelberg, 1958.
[15] G. R. Irwin, 'Analysis of Stresses and Strains Near the End of a Crack Traversing a Plate', *J Appl Mech*, vol. 24, no. 3, pp. 361–364, Sep. 1957, doi: 10.1115/1.4011547.
[16] A. Trudel, M. Turgeon, E. Aecom, C. East, and I. Lanctôt, 'Recent trends in the design of hydropower components subjected to cycling and fatigue; towards improved technical design specifications', 2017. [Online]. Available: https://www.researchgate.net/publication/320310804
[17] F. V. Antunes, S. Serrano, R. Branco, and P. Prates, 'Fatigue crack growth in the 2050-T8 aluminium alloy', *Int J Fatigue*, vol. 115, pp. 79–88, Oct. 2018, doi: 10.1016/J.IJFATIGUE.2018.03.020.
[18] ELBER W, 'Fatigue crack closure under cyclic tension', *Eng Fract Mech*, vol. 2, no. 1, pp. 37–45, Jul. 1970, doi: 10.1016/0013-7944(70)90028-7.
[19] W. Elber, 'The Significance of Fatigue Crack Closure', *ASTM Special Technical Publication*, vol. STP 486, pp. 230–242, 1971, doi: 10.1520/STP26680S.
[20] L. P. Borrego, J. M. Ferreira, and J. M. Costa, 'Fatigue crack growth and crack closure in an AlMgSi alloy', *Fatigue Fract Eng Mater Struct*, vol. 24, no. 4, pp. 255–265, Apr. 2001, doi: 10.1046/J.1460-2695.2001.00383.X.
[21] L. P. Borrego, J. M. Ferreira, J. M. Pinho da Cruz, and J. M. Costa, 'Evaluation of overload effects on fatigue crack growth and closure', *Eng Fract Mech*, vol. 70, no. 11, pp. 1379–1397, Jul. 2003, doi: 10.1016/S0013-7944(02)00119-4.
[22] R. O. Ritchie, S. Suresh, and C. M. Moss, 'Near-Threshold Fatigue Crack Growth in 2 1/4 Cr-1Mo Pressure Vessel Steel in Air and Hydrogen', *J Eng Mater Technol*, vol. 102, no. 3, pp. 293–299, Jul. 1980, doi: 10.1115/1.3224813.
[23] S. Suresh and R. O. Ritchie, 'On the influence of fatigue underloads on cyclic crack growth at low stress intensities', *Materials Science and Engineering*, vol. 51, no. 1, pp. 61–69, Nov. 1981, doi: 10.1016/0025-5416(81)90107-5.
[24] S. SURESH and R. O. RITCHIE, 'GEOMETRIC MODEL FOR FATIGUE CRACK CLOSURE INDUCED BY FRACTURE SURFACE ROUGHNESS.', *METALL TRANS A*, vol. V 13A, no. N 9, pp. 1627–1631, 1982, doi: 10.1007/BF02644803/METRICS.
[25] A. Wells, 'Unstable crack propagation in metals: cleavage and fast fracture', in *Proceedings of the crack propagation symposium*, 1961, p. 26028.
[26] J. R. Rice, 'A Path Independent Integral and the Approximate Analysis of Strain Concentration by Notches and Cracks', *J Appl Mech*, vol. 35, no. 2, pp. 379–386, Jun. 1968, doi: 10.1115/1.3601206.
[27] X. K. Zhu, P. Zelenak, and T. McGaughy, 'Comparative study of CTOD-resistance curve test methods for SENT specimens', *Eng Fract Mech*, vol. 172, pp. 17–38, Mar. 2017, doi: 10.1016/J.ENGFRACMECH.2017.01.007.
[28] B. Marques, L. P. Borrego, J. M. Ferreira, F. V. Antunes, and R. Branco, 'A numerical analysis of fatigue crack closure using CTOD', *Procedia Structural Integrity*, vol. 18, pp. 645–650, Jan. 2019, doi: 10.1016/J.PROSTR.2019.08.211.
[29] F. V. Antunes, R. Branco, P. A. Prates, and L. Borrego, 'Fatigue crack growth modelling based on CTOD for the 7050-T6 alloy', *Fatigue Fract Eng Mater Struct*, vol. 40, no. 8, pp. 1309–1320, Aug. 2017, doi: 10.1111/FFE.12582.
[30] C. M. Ward-Close, A. F. Blom, and R. O. Ritchie, 'Mechanisms associated with transient fatigue crack growth under variable-amplitude loading: An

experimental and numerical study', *Eng Fract Mech*, vol. 32, no. 4, pp. 613–638, Jan. 1989, doi: 10.1016/0013-7944(89)90195-1.

[31] C. Laird and G. C. Smith, 'Crack propagation in high stress fatigue', *Philosophical Magazine*, vol. 7, no. 77, pp. 847–857, 1962, doi: 10.1080/14786436208212674.

[32] R. M. N. Pelloux, 'Crack extension by alternating shear', *Eng Fract Mech*, vol. 1, no. 4, pp. 697–704, Apr. 1970, doi: 10.1016/0013-7944(70)90008-1.

[33] Subra Suresh, *Fatigue of Materials*. 1991. Accessed: Jun. 19, 2024. [Online]. Available: https://books.google.pt/books?hl=pt-PT&lr=&id=j4w6frFAiQcC&oi=fnd&pg=PR17&ots=Ac7qNFfEbG&sig=k905xkOqkWI7sBDLyuJz6fhyPkk&redir_esc=y#v=onepage&q&f=false

[34] V. Tvergaard, 'Overload effects in fatigue crack growth by crack-tip blunting', in *International Journal of Fatigue*, Oct. 2005, pp. 1389–1397. doi: 10.1016/j.ijfatigue.2005.06.003.

[35] D. Cojocaru and A. M. Karlsson, 'Assessing plastically dissipated energy as a condition for fatigue crack growth', *Int J Fatigue*, vol. 31, no. 7, pp. 1154–1162, Jul. 2009, doi: 10.1016/J.IJFATIGUE.2008.12.009.

[36] J. B. Baptista, F. V. Antunes, L. Correia, and R. Branco, 'A numerical study of the effect of single overloads on plasticity induced crack closure', *Theoretical and Applied Fracture Mechanics*, vol. 88, pp. 51–63, Apr. 2017, doi: 10.1016/j.tafmec.2016.12.001.

[37] Ö. Vardar, 'Effect of single overload in FCP', *Eng Fract Mech*, vol. 30, no. 3, pp. 329–335, Jan. 1988, doi: 10.1016/0013-7944(88)90191-9.

[38] X. Zheng, H. Cui, C. C. Engler-Pinto, X. Su, and W. Wen, 'Numerical modeling of fatigue crack propagation based on the theory of critical distances: Effects of overloads and underloads', *Eng Fract Mech*, vol. 128, no. C, pp. 91–102, 2014, doi: 10.1016/j.engfracmech.2014.07.006.

[39] C. M. Ward-Close, A. F. Blom, and R. O. Ritchie, 'Mechanisms associated with transient fatigue crack growth under variable-amplitude loading: An experimental and numerical study', *Eng Fract Mech*, vol. 32, no. 4, pp. 613–638, Jan. 1989, doi: 10.1016/0013-7944(89)90195-1.

[40] P. Heuler and H. Klätschke, 'Generation and use of standardised load spectra and load–time histories', *Int J Fatigue*, vol. 27, no. 8, pp. 974–990, Aug. 2005, doi: 10.1016/J.IJFATIGUE.2004.09.012.

[41] J. M. Potter and R. T. Watanabe, *Development of fatigue loading spectra*, vol. 1006. ASTM International, 1989.

[42] J. B. de Jong, D. Schütz, H. Lowak, and J. Schijve, 'A standardized load sequence for flight simulation tests on transport aircraft wing structures', *NLR-TR 73029 U, LBF Bericht FB-106*, 1973, Accessed: Jun. 20, 2024. [Online]. Available: https://repository.tudelft.nl/islandora/object/uuid%3Ade6e293c-034f-426d-b842-3229268fd7ac

[43] R. Bao and X. Zhang, 'Fatigue crack growth behaviour and life prediction for 2324-T39 and 7050-T7451 aluminium alloys under truncated load spectra', *Int J Fatigue*, vol. 32, no. 7, pp. 1180–1189, Jul. 2010, doi: 10.1016/J.IJFATIGUE.2009.12.010.

[44] J. Silva, 'Relatório do Tirocínio ENGAER', *Força Aérea Portuguesa*, 2003.

[45] M. Yamamoto, K. Makino, and H. Ishiduka, 'Experimental validation of railway axle fatigue crack growth using operational loading', *Eng Fract Mech*, vol. 213, pp. 142–152, May 2019, doi: 10.1016/J.ENGFRACMECH.2019.04.001.
[46] Rob. Tardif, Ontario. Ministry of Transportation., and GFR Consulting., '1995 COMMERCIAL VEHICLE SURVEY: STATION SUMMARY REPORT', p. 313, Dec. 1997.
[47] L. He, H. Akebono, M. Kato, and A. Sugeta, 'Fatigue life prediction method for AISI 316 stainless steel under variable-amplitude loading considering low-amplitude loading below the endurance limit in the ultrahigh cycle regime', *Int J Fatigue*, vol. 101, pp. 18–26, Aug. 2017, doi: 10.1016/J.IJFATIGUE.2017.04.006.
[48] J. A. Harter, 'Comparison of contemporary FCG life prediction tools', *Int J Fatigue*, vol. 21, no. SUPPL. 1, pp. S181–S185, Sep. 1999, doi: 10.1016/S0142-1123(99)00070-5.
[49] J. C. Newman, *A crack-closure model for predicting fatigue crack growth under aircraft spectrum loading*, vol. 748. ASTM International West Conshohocken, PA, 1981.
[50] M. Creager, 'Personal Conversations with James A', *Harter, Northrop Corporation, Pico Rivera, CA*, vol. 1983, 1982.
[51] R. Sunder, 'Personal Conversations with James A', *Harter, US Air Force Materials Directorate, Wright-Patterson, AFB, OH*, vol. 1989, 1988.
[52] J. A. Harter, 'AFGROW users guide and technical manual', *Air Force Research Laboratory*, vol. 10, 1999.
[53] P. Heuler and T. Seeger, 'A criterion for omission of variable amplitude loading histories', *Int J Fatigue*, vol. 8, no. 4, pp. 225–230, Oct. 1986, doi: 10.1016/0142-1123(86)90025-3.
[54] M. Matsuishi and T. Endo, 'Fatigue of metals subject to varying stress', *Japan Society of Mechanical Engineers, Fukuoka, Japan*, vol. 68, no. 2, pp. 37–40, 1968.
[55] S. D. Downing and D. F. Socie, 'Simple rainflow counting algorithms', *Int J Fatigue*, vol. 4, no. 1, pp. 31–40, Jan. 1982, doi: 10.1016/0142-1123(82)90018-4.
[56] 'A Cycle Counting Algorithm for Fatigue Damage Analysis on JSTOR'. Accessed: Jul. 05, 2024. [Online]. Available: https://www.jstor.org/stable/44734430?seq=1
[57] C. Amzallag, J. P. Gerey, J. L. Robert, and J. Bahuaud, 'Standardization of the rainflow counting method for fatigue analysis', *Int J Fatigue*, vol. 16, no. 4, pp. 287–293, Jun. 1994, doi: 10.1016/0142-1123(94)90343-3.
[58] Y.-L. Lee, M. E. Barkey, and H.-T. Kang, *Metal fatigue analysis handbook: practical problem-solving techniques for computer-aided engineering*. Elsevier, 2011.
[59] S. Beretta and M. Carboni, 'Variable amplitude fatigue crack growth in a mild steel for railway axles: Experiments and predictive models', *Eng Fract Mech*, vol. 78, no. 5, pp. 848–862, Mar. 2011, doi: 10.1016/J.ENGFRACMECH.2010.11.019.
[60] M. Rieger *et al.*, 'Fatigue crack growth in full-scale railway axles – Influence of secondary stresses and load sequence effects', *Int J Fatigue*, vol. 132, p. 105360, Mar. 2020, doi: 10.1016/J.IJFATIGUE.2019.105360.

[61] M. Luke, I. Varfolomeev, K. Lütkepohl, and A. Esderts, 'Fatigue crack growth in railway axles: Assessment concept and validation tests', *Eng Fract Mech*, vol. 78, no. 5, pp. 714–730, Mar. 2011, doi: 10.1016/J.ENGFRACMECH.2010.11.024.
[62] M. Luke, I. Varfolomeev, K. Lütkepohl, and A. Esderts, 'Fracture mechanics assessment of railway axles: Experimental characterization and computation', *Eng Fail Anal*, vol. 17, no. 3, pp. 617–623, Apr. 2010, doi: 10.1016/J.ENGFAILANAL.2009.04.008.
[63] M. Aursand, G. T. Frøseth, P. J. Haagensen, and B. H. Skallerud, 'Crack growth in high strength mooring line steel under variable amplitude loading', *Marine Structures*, vol. 93, Jan. 2024, doi: 10.1016/j.marstruc.2023.103534.
[64] ASTM E 1049-85, *Standard practices for cycle counting in fatigue analysis*. 2011.
[65] P. Lequeu, K. P. Smith, and A. Danié, 'Aluminum-Copper-Lithium Alloy 2050 Developed for Medium to Thick Plate', doi: 10.1007/s11665-009-9554-z.
[66] H. W. Swift, 'Plastic instability under plane stress', *J Mech Phys Solids*, vol. 1, no. 1, pp. 1–18, Oct. 1952, doi: 10.1016/0022-5096(52)90002-1.
[67] J. Lemaitre and J.-L. Chaboche, 'Mechanics of Solid Materials', *Mechanics of Solid Materials*, Feb. 1990, doi: 10.1017/CBO9781139167970.
[68] P. J. Armstrong and C. O. Frederick, 'CEGB Report RD/B/N 731', *Berkeley Nuclear Laboratories*, 1966.
[69] L. F. Menezes and C. Teodosiu, 'Three-dimensional numerical simulation of the deep-drawing process using solid finite elements', *J Mater Process Technol*, vol. 97, no. 1–3, pp. 100–106, Jan. 2000, doi: 10.1016/S0924-0136(99)00345-3.
[70] M. C. Oliveira, J. L. Alves, and L. F. Menezes, 'Algorithms and strategies for treatment of large deformation frictional contact in the numerical simulation of deep drawing process', *Archives of Computational Methods in Engineering*, vol. 15, no. 2, pp. 113–162, 2008, doi: 10.1007/s11831-008-9018-x.
[71] M. F. Borges, D. M. Neto, and F. V. Antunes, 'Numerical simulation of fatigue crack growth based on accumulated plastic strain', *Theoretical and Applied Fracture Mechanics*, vol. 108, p. 102676, Aug. 2020, doi: 10.1016/J.TAFMEC.2020.102676.
[72] M. F. Borges *et al.*, 'Fatigue crack propagation analysis in 2024-T351 aluminium alloy using nonlinear parameters', *Int J Fatigue*, vol. 153, p. 106478, Dec. 2021, doi: 10.1016/J.IJFATIGUE.2021.106478.
[73] M. A. Miner, 'Cumulative Damage in Fatigue', *J Appl Mech*, vol. 12, no. 3, pp. A159–A164, Sep. 1945, doi: 10.1115/1.4009458.
[74] B. S. ISO, '12108, 2002:'Metallic materials-Fatigue testing-Fatigue crack growth method'', *British Standards Institution, London*, 2003.
[75] A. S. for T. and Materials, *Standard test method for measurement of fatigue crack growth rates: designation: E 647-08*. ASTM international, 2008.
[76] S. Suresh, G. F. Zamiski, and D. R. O. Ritchie, 'Oxide-Induced Crack Closure: An Explanation for Near-Threshold Corrosion Fatigue Crack Growth Behavior', *Metallurgical Transactions A*, vol. 12, no. 8, pp. 1435–1443, Aug. 1981, doi: 10.1007/BF02643688/METRICS.

ANNEX A

	LF		LF		LF		LF
0	0.000748	30	0.248322	60	0.005028	90	0.004841
1	0.043841	31	0.564087	61	0.037886	91	0.533267
2	0.011203	32	0.004944	62	0.017334	92	0.255047
3	0.670501	33	0.037869	63	0.526724	93	0.295556
4	0.033925	34	0.019062	64	0.25431	94	0.163377
5	0.635144	35	0.536713	65	0.370726	95	0.554579
6	0.311546	36	0.259467	66	0.248322	96	0.005433
7	0.459793	37	0.313772	67	0.564087	97	0.040751
8	0.262297	38	0.198067	68	0.004944	98	0.02027
9	0.568384	39	0.557581	69	0.037869	99	0.532122
10	0.004986	40	0.00507	70	0.019062	100	0.264081
11	0.038068	41	0.530109	71	0.536713	101	0.488082
12	0.009582	42	0.255763	72	0.259467	102	0.328235
13	0.540951	43	0.410124	73	0.313772	103	0.650774
14	0.265009	44	0.262297	74	0.198067	104	0.043317
15	0.338374	45	0.568384	75	0.557581	105	1
16	0.226452	46	0.004986	76	0.00507	106	0.663735
17	0.560582	47	0.038068	77	0.530109	107	0.67932
18	0.004841	48	0.009582	78	0.255763	108	0.273733
19	0.533267	49	0.540951	79	0.410124	109	0.675425
20	0.258435	50	0.265009	80	0.262297	110	0.024241
21	0.295625	51	0.338374	81	0.568384	111	0.729614
22	0.163167	52	0.226452	82	0.004986	112	0.014254
23	0.554563	53	0.560582	83	0.038068	113	0.059203
24	0.005028	54	0.004841	84	0.009582	114	0.027493
25	0.037886	55	0.533267	85	0.540951		
26	0.017334	56	0.258435	86	0.265009		
27	0.526724	57	0.295625	87	0.338374		
28	0.25431	58	0.163167	88	0.226452		
29	0.370726	59	0.554563	89	0.560582		

Annex A: Load factors defining the load pattern A.

ANNEX B

	LF		LF		LF		LF
0	0.000000	43	0.966835	86	0.438201	129	1.000000
1	0.286178	44	0.836106	87	0.739513	130	0.501917
2	0.265704	45	0.977408	88	0.625141	131	0.653534
3	0.806195	46	0.479213	89	0.832263	132	0.537162
4	0.514104	47	0.629231	90	0.717089	133	0.697034
5	0.651896	48	0.519832	91	0.881887	134	0.595594
6	0.530600	49	0.671238	92	0.763241	135	0.826455
7	0.694926	50	0.585274	93	0.905380	136	0.687306
8	0.583734	51	0.822092	94	0.780386	137	0.828957
9	0.805616	52	0.668782	95	0.907818	138	0.723355
10	0.685107	53	0.956836	96	0.544427	139	0.989214
11	0.839936	54	0.824043	97	0.682619	140	0.490376
12	0.729971	55	0.964528	98	0.566148	141	0.641797
13	0.864084	56	0.468641	99	0.730588	142	0.528426
14	0.746465	57	0.616118	100	0.616719	143	0.684210
15	0.872290	58	0.511096	101	0.831068	144	0.590154
16	0.512407	59	0.835967	102	0.710533	145	0.824411
17	0.662406	60	0.737533	103	0.869216	146	0.678452
18	0.545455	61	0.913171	104	0.753744	147	0.966835
19	0.709035	62	0.792737	105	0.890818	148	0.836106
20	0.601776	63	0.945602	106	0.769169	149	0.977408
21	0.828228	64	0.813184	107	0.894329	150	0.479213
22	0.695515	65	0.950757	108	0.529287	151	0.629231
23	0.842315	66	0.458498	109	0.673903	152	0.519832
24	0.734087	67	0.602919	110	0.555528	153	0.671238
25	1.000000	68	0.501986	111	0.720447	154	0.585274
26	0.501917	69	0.834557	112	0.608775	155	0.822092
27	0.653534	70	0.730890	113	0.829755	156	0.668782
28	0.537162	71	0.903993	114	0.703196	157	0.804033
29	0.697034	72	0.782130	115	0.855901	158	0.698995
30	0.595594	73	0.933122	116	0.744130	159	0.817906
31	0.826455	74	0.802157	117	0.876312	160	0.701427
32	0.687306	75	0.936440	118	0.757393	161	0.836728
33	0.828957	76	0.448441	119	0.881756	162	0.625496
34	0.723355	77	0.747388	120	0.515049	163	0.752831
35	0.989214	78	0.635239	121	0.664228	164	0.677530
36	0.490376	79	0.833361	122	0.546327	165	0.809238
37	0.641797	80	0.724075	123	0.709213	166	0.724216

38	0.528426	81	0.893569	124	0.601776	167	0.853318
39	0.684210	82	0.772769	125	0.828228	168	0.042090
40	0.590154	83	0.919610	126	0.695515	169	0.060834
41	0.824411	84	0.791314	127	0.842315	170	0.000000
42	0.678452	85	0.921994	128	0.734087		

Annex B Load factors defining the load pattern B.